Predicting atmospheric propagation of radio frequency waves using meteorological data and the split-step parabolic equation

ERIK NILSSON
MASTER´S THESIS
DEPARTMENT OF ELECTRICAL AND INFORMATION TECHNOLOGY
FACULTY OF ENGINEERING | LTH | LUND UNIVERSITY

Predicting atmospheric propagation of radio frequency waves using meteorological data and the split-step parabolic equation

Erik Nilsson
er1185ni-s@student.lu.se

Department of Electrical and Information Technology
Lund University

Supervisor: Daniel Sjöberg

Examiner: Mats Gustafsson

March 15, 2026

Printed in Sweden
Tryckeriet i E-huset, Lund

Abstract

This thesis, along with the Propagation Predictor written in MATLAB, offers a quick and easy way of predicting how Electromagnetic (EM)-waves will propagate given the current atmospheric situation . While the thesis is written with the goal of explaining choice and phenomena, the Propagation Predictor is built with the goal of not requiring deep knowledge of neither EM-waves nor meteorology.

Meteorological data is used to predict tropospheric propagation of EM-waves in the Radio Frequency (RF) spectrum. Theory for EM-waves, meteorology and atmospheric refractivity is presented, as well as the mathematics required for the simulation.

The simulation is done using a wide angle approximation Split Step Parabolic Equation (SSPE). Polarization is ignored and the treatment of reflections is simplified. Attenuation from air, precipitation, and condensation is calculated from the same data as the propagation.

The MATLAB program written (the Propagation Predictor) demonstrates a feasible approach for how meteorological data can be used in predicting the propagation of RF based sensor systems. While the SSPE is an established approach, previous works suggest that the vertical fidelity of meteorological data is too low for accurately recreating the atmospheric layers. In addition to this, reflections, especially for rough terrain, risk being to simplified for accuracy. Comparison to a similar model shows deviations, indicating that the simulation is not entirely accurate.

Declaration

I hereby affirm that this Master thesis was composed by myself, that the work herein is my own except where explicitly stated otherwise in the text. This work has not been submitted for any other degree or professional qualification except as specified; nor has it been published. Where other people's work has been used (either from a printed source, internet, or any other source), this has been carefully acknowledged and referenced.

In certain parts of this thesis, AI assistance (OpenAI's GPT-5) has been employed. Its main contribution has been in editorial tasks, such as importing values to tables or creating templates to keep the graphical profile consistent. In some cases, the process resembled a "Ship of Theseus" scenario—where the AI initially produced largely non-functional code, which was then iteratively revised and rewritten through numerous small modifications until the final version was entirely transformed.

Acknowledgements

I want to thank my supervisor at LTH, Daniel Sjöberg, for invaluable help and patience in explaining difficult concepts, as well as for his input on structure and on which areas are relevant.

I am also grateful for the support from my supervisor at Combitech, Jon Staffeldt, as well as Kent Adolfsson and Esbjörn Olsson whose input regarding meteorology and data sets have helped immensely.

Abbreviations

DMFT Discrete Mixed Fourier Transform

ECMWF European Centre for Medium-Range Weather Forecasts (Global NWP provider)

EM Electromagnetic (Refers to EM waves or spectrum)

FAI Fédération Aéronautique Internationale

FEM Finite Element Method

FOI the Swedish Defence Research Agency (Totalförsvarets forskningsintitut)

GRIB General Regularly-distributed Information in Binary

MEPS Meteorological Ensemble Prognosis System

NAPE Narrow Angle approximation

PE Parabolic Equation (Mathematical approximation)

Radar Radio Detection and Ranging (Active remote sensing system)

RF Radio Frequency (3 Hz – 3 THz)

RRE Radar Range Equation (Relates power range and detectability)

RT Ray Tracing (High-frequency propagation method)

SMHI Swedish Meteorological and Hydrological Institute

SSPE Split-Step Parabolic Equation (Wave propagation modeling method)

WAPE Wide Angle approximation

Popular Science Summary

If you go to the ocean and look out along the horizon, you might see boats. They can appear behind, on top of or in front of the horizon, and on some days they might even appear to be floating above it. This illusion, or mirage, comes from light being bent, meaning that the boat you see is not in a straight line from your eyes. These mirages are standard for radars, but sometimes the mirage has a larger effect than expected. This is called an anomaly.

For you, seeing a flying boat over the horizon doesn't matter much. You know that boats can't fly, and can easily recognize it as a mirage. For radars this is harder, and it might not even be a boat that's observed; seeing an aeroplane, how can one be certain of its altitude?

In order to better understand the mirages, we can use weather data for the place we're looking at. The weather is what causes the anomalies, so by simulating how light will travel through the air we get a clearer view of what is real.

SMHI has a lot of data available on their website, and the type called MEPS contains all that is needed and more. By choosing to extract temperature, pressure, humidity, cloud and rain, we can calculate how much the air should bend the light, given the current weather. Here we can also modify the values a bit, in order to treat the earth as flat. However, guessing how the light is bent just by looking at different values is often just that - guessing - so in order to get better predictions we need to simulate the light.

How light behaves is well known, but using the fully correct models is very difficult. Instead, we set limitations to make calculations easier. First, we say that light only travels in a cone; instead of a lightbulb we simulate a headlight. We then say that this headlight can only point in one direction (forward) and that it can't be tilted up or down too much. Finally, we put a piece of paper along the light beam from the headlight, and choose to only simulate how it looks on that piece of paper.

The end product of this is slices showing how strong the light is at different distances and different heights. Going back to the initial analogy, this can give an indication of where the flying boat is most likely to be.

Table of Contents

List of Figures

List of Tables

Chapter 1
Background

In an increasingly hostile and electronic world, with the fiber-optic cables of drones covering Ukraine like spiderwebs and rockets crossing European borders, knowing what happens in the atmosphere is of great importance. The government of Sweden seems to agree, as allegedly 10 billion SEK has been put towards new sensor systems [4].

Whether active or passive sensors, both are subject to the effects of atmospheric refraction. The rule of thumb for Radio Frequency (RF) based sensor systems is that the radar horizon is slightly further away than the optical horizon, following the effective earth model [3, p.164]. This effect stems from the assumption of a standard atmosphere, an assumption not necessarily correct.

On April 13 2022, two explosions occurred aboard the Russian warship Moskva, leading to it sinking the next day. Ukraine claims these explosions are the result of two missiles fired from shore, acquiring radar lock on the ship. Estimates put the ship at a distance of roughly 135km at the time of impact, with Ukrainan radars having an operable range of 46km. Reference [5] finds that radar-lock was possible, given the atmospheric conditions at the time.

When atmospheric conditions are not standard, the effective earth model fails and other methods of prediction must be used. One such approach is simulating the wave propagation through a model of the atmosphere. This data can come from readily available meteorological data, as this contains all parameters necessary to predict propagation. Having this more detailed propagation model also allows for better range assessment when using passive sensors.

Chapter 2
General Theory

The basis for this thesis is Electromagnetic (EM) waves and their interactions with the atmosphere. As such, the theory will begin by explaining electromagnetism, continue with Earth and space weather, and tie them both together.

2.1 Electromagnetism

In 1864, James Clerk Maxwell published equations relating the concepts electricity and magnetism. These were later re-written in vector form by Oliver Heaviside, and those are the equations that today are known as Maxwell's equations.

2.1.1 Maxwell's equations

Maxwell's equations give all information necessary to calculate how an EM wave will propagate, regardless of whether the wave is the signal from a long-wave antenna (< 300kHz) or the beam from a green laser pointer (563.5THz):

$$\nabla \cdot \mathbf{E} = \frac{\rho}{\epsilon_0} \tag{2.1}$$

$$\nabla \cdot \mathbf{B} = 0 \tag{2.2}$$

$$\nabla \times \mathbf{E} = -\frac{\partial \mathbf{B}}{\partial t} \tag{2.3}$$

$$\nabla \times \mathbf{B} = \mu_0 \left(\mathbf{J} + \epsilon_0 \frac{\partial \mathbf{E}}{\partial t} \right) \tag{2.4}$$

The equations above are applicable to vacuum. As is standard notation, $\mathbf{E}$ is the electric field strength, $\mathbf{B}$ is the magnetic flux density, ρ is the charge density, and $\mathbf{J}$ is the current density. However, using these equations to actually calculate something is computationally demanding, and can often be avoided by choosing appropriate approximations and simplifications. A common situation is that there are no sources present (free space), which sets ρ and $\mathbf{J}$ to zero.

A useful tool to visualise propagation is ray optics. It is a reasonable approach when propagation occurs over many wavelengths, as the EM-wave will behave as a beam, or ray. This can be used to get an intuitive feel for how the wave will behave.

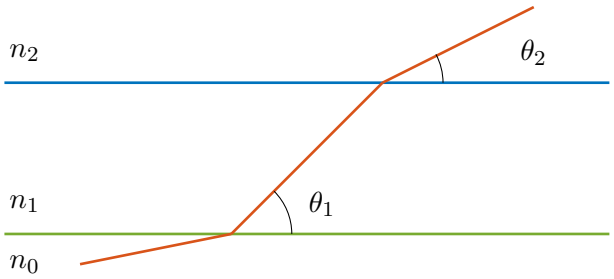

Figure 2.1: When light moves through different refractive indices, it is bent according to Snell's law. The figure shows a beam of light entering from below and passing two index changes. Given the angles present it can be seen that $n_0 < n_2 < n_1$.

2.1.2 Refractive index and Snell's law

The refractive index n of a material is a unit-less value describing its phase velocity v relative to the speed of light in vacuum c, $n \equiv \frac{c}{v} = \sqrt{\mu_\mathrm{r}\epsilon_\mathrm{r}}$, where μ_r is the relative permeability and ϵ_r is the relative permittivity of the medium the wave is propagating in [6, p.189]. In general, n is wavelength dependent $\big(n = n(\lambda)\big)$ though wavelength independent approximations can be made for certain bands under certain conditions, see Section 2.3.1.

Refractive index n is very useful in optics, where Snell's law[1]

$$n_1 \cos\theta_1 = n_2 \cos\theta_2 \tag{2.5}$$

can be used to calculate how light will be refracted when moving from one medium to another[6, p.202]. Though technically only slowing down the light, the different phase velocities in the two media causes the wavefront to pivot so that the propagation direction of the wave changes.

One variation of Snell's law is Snell's law for polar coordinates, [2, p.87]

$$n_1 r_1 \cos\theta_1 = n_2 r_2 \cos\theta_2 \tag{2.6}$$

which describes light refracting between two curved surfaces, see Figure 2.2. The surfaces need to be close together and the angles need to be small in order for the equation to be viable; large angles would negate the effect of the curvature, making Snell's law for flat geometry viable. At the same time, too large distance between the layers would cause an unreasonable difference in grazing angle for the two surfaces.

2.1.3 Polarization

Writing the wave equation for an RF wave,

$$\mathbf{E}(\mathbf{r}, t) = \mathbf{E}_0 \cos(\omega t - nkx) \tag{2.7}$$

[1] Though Snell's law usually is described using the angle of incidence (toward the normal), here we use the grazing angle as that is most common in literature on atmospheric refractivity.

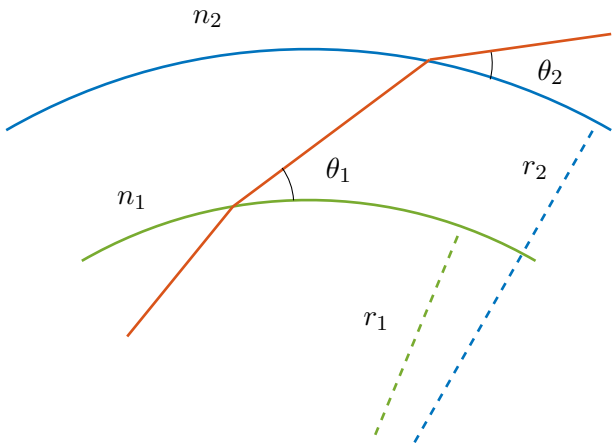

Figure 2.2: Snells law for polar coordinates. It requires that both distance and angles are small. If the center of the curves were the center of Earth, the source would need to point along the horizon for the formula to be relevant.

the $\mathbf{E_0}$ part corresponds to the wave's polarization. The polarization is the direction in which the wave amplitude changes, and for EM-waves it is always orthogonal to the propagation direction. Given a propagation direction in $\hat{x}$, polarization can then be in a combination of $\hat{y}$ and $\hat{z}$, or horizontal and vertical. Reflections from a plane parallel to the polarization are usually stronger than non-parallel [7].

In equation (2.7), n and k are also present. The refractive index n is the ratio between the wavelength in vacuum and the wavelength in the material, and k is the wave number in vacuum. The refractive index is the part responsible for different behaviour in different media.

2.1.4 Active sensors

The most common active sensor system is the Radio Detection and Ranging (Radar). It works by transmitting an RF-pulse and analyses the wave that is reflected back. A frequency-change (Doppler shift) in the received signal can be used to calculate the velocity of the target, and the distance can be calculated from $R = \frac{c\Delta T}{2}$, with c being the speed of light and ΔT the time between sending and receiving.

Beside affecting the range calculation, the two-way propagation also affects the spread of the signal. An antenna in sensor applications is often designed to have a narrow beam-width. However, no matter how narrow, the signal strength will spread and and dissipate the further it extends from the source. This decrease in power density follows $P \propto (4\pi R^2)^{-1}$, in the same way that the area of a sphere increases with increased radius. After the reflection in the target, the same sort of spread happens. As such it is commonplace to use $P \propto ((4\pi)^2 R^4)^{-1}$ in regards to active sensors, using the one-way distance R.

2.1.5 Passive sensors

A second alternative to gathering information is using passive sensors. These follow the same limitations regarding attenuation (see Sections 2.1.6) as active sensors, with the difference that they only receive signals and never transmit. Because of this both range and velocity of the target is difficult to ascertain. What can be gathered however is signal strength, polarization, frequency and angle of arrival.

With known sources and good models showing expected attenuation, signal strength can be used to approximate possible distance. Polarization and frequency can be compared to known sources to further identify the signal. As will be seen in Section 2.3.4, atmospheric layers can cause EM-waves to be bent towards the Earth, reflect against a body of water, and do so continuously. It is reasonable to expect that these reflections attenuate vertically polarized waves more than horizontally polarized waves, due to the total transmission of vertically polarized EM waves at the Brewster angle. That said, when observing ground clutter using an active sensor, the strength of the returning signal was shown to be largely independent of polarization [8]. This source does however not mention whether this required reflections or not.

2.1.6 Attenuation

Attenuation limits the range of both active and passive sensors. Often described as two-way - that is to say, twice as large in order to capture the attenuation for back-and-forth while only using the range from start to finish - and in the unit decibel in order to simplify calculations, it shows how much signal strength is lost when propagating through different regions. In the Radar Range Equation (RRE)[2]

$$\mathrm{SNR} = \frac{P_\mathrm{t} G_\mathrm{t} G_\mathrm{r} \lambda^2 \sigma}{(4\pi)^3 R^4 k T_0 F_\mathrm{s} B L_\mathrm{s}} \tag{2.8}$$

the attenuation is included in the total system loss, L_s, which contains the factor L_t^2, where L_t is the one-way propagation loss. For the rest of the thesis only one-way propagation will be used.

The transmit losses is the total of many sections, $L_\mathrm{t}[\mathrm{dB}] = \sum_1^N L_\mathrm{tn}$, where each section is the attenuation $\alpha_\mathrm{n}[\mathrm{dB/km}]$ times the propagation distance $d_\mathrm{n}[\mathrm{km}]$. Attenuation differs for different media and is caused by scattering and absorption. Scattering is dependent on electrical size[3] and particulate density, while absorption is only affected by the particulate density [3, p.147].

Inversely related to the one-way transmit losses L_t is the propagation factor, $F = L_\mathrm{t}^{-1}$. The propagation factor F is defined from how much of the power of an

[2]Here described as Signal-to-Noise Ratio, it shows how much of the original signal is expected to come back with regards to initial power P_t, gain of antenna and receiver G_t and G_r, wavelength λ, radar cross section σ of the target, one-way distance R, thermal noise $kT_0F_\mathrm{s}B$ and system losses L_s.

[3]The electrical size is the relation between wavelength and object size. Objects smaller than the wavelength cause less scattering the smaller they are, while objects between one and ten wavelengths in size cause fluctuating scattering until smoothing out at a constant value. These regions are called Rayleigh, Mie and optical, respectively.

initial wave A_0 is weakened, $F = A/A_0$, given a propagated wave power A. It is also calculated using the attenuation coefficient α and the propagation distance d.

Since $F[\text{dB}] = -\alpha[\text{dB/km}] \cdot d[\text{km}]$, and the conversion from linear to decibel is $F[\text{lin}] = 10\log_{10}(F[\text{dB}])$, the linear one-way propagation factor is

$$F[\text{lin}] = 10^{-0.1\alpha[\text{dB/km}]\cdot d[\text{km}]} \tag{2.9}$$

where α[dB/km] is the one-way attenuation coefficient.

Atmospheric gases

In the 100 MHz to 50 GHz range, absorption is mostly caused by the atmospheric gases oxygen and water vapour [2, p.270]. The one-way attenuation [dB/km] for oxygen is

$$\alpha_{\text{oxygen}} = \frac{0.34}{\lambda'^2}\left[\frac{0.018}{\frac{1}{\lambda'^2} + 0.018^2} + \frac{0.049}{\left(2 + \frac{1}{\lambda'}\right)^2 + 0.049^2} + \frac{0.049}{\left(2 - \frac{1}{\lambda'}\right)^2 + 0.049^2}\right] \tag{2.10}$$

and for water vapour

$$\frac{\alpha_{\text{water}}}{\rho} = \frac{3.5 \cdot 10^{-3}}{\lambda'^2}\left[\frac{0.087}{\left(\frac{1}{\lambda'} - \frac{1}{1.35}\right)^2 + 0.087^2} + \frac{0.087}{\left(\frac{1}{\lambda'} + \frac{1}{1.35}\right)^2 + 0.087^2}\right] \tag{2.11}$$

where λ' is the wavelength in centimetres for both equations, and ρ is the absolute humidity [g/m^3]. While ρ is not strictly temperature dependant, warmer air can hold more water [9], leading to potentially larger attenuation at higher temperatures.

The oxygen attenuation is sometimes called the "0.5 cm line" and the water attenuation the "1.35 cm line" as they have local maxima at wavelengths of 0.5 cm and 1.35 cm (≈60 GHz and ≈22 GHz) and respectively. These two effects are often visualized together, as seen in Figure 2.3.

Clouds

The attenuation from clouds or fog is negligible for frequencies below 5 GHz ($\lambda > 6$ cm) [2, p.291]. Above 5 GHz the one-way attenuation α_{cloud} [dB/km] follows

$$\alpha_{\text{cloud}} = \rho'\left(-1.347 + 0.66f + \frac{11.152}{f} - 0.022T\right) \tag{2.12}$$

with ρ' being liquid water concentration [g/m^3], f the frequency [GHz] and T the temperature [°C] [3, p.155]. It is worth noting that absolute humidity ρ mentioned in Section 2.1.6 is not the same as liquid water concentration ρ'. The absolute humidity ρ is the mass of gaseous water in the air, while ρ' is the mass of condensed (liquid or frozen) water. This concentration differs depending on where condensation happens, see Table 2.1. Radiation fog appears when the Earths radiation cooling is below dew level and advection fog is from cold air passing over a colder surface.

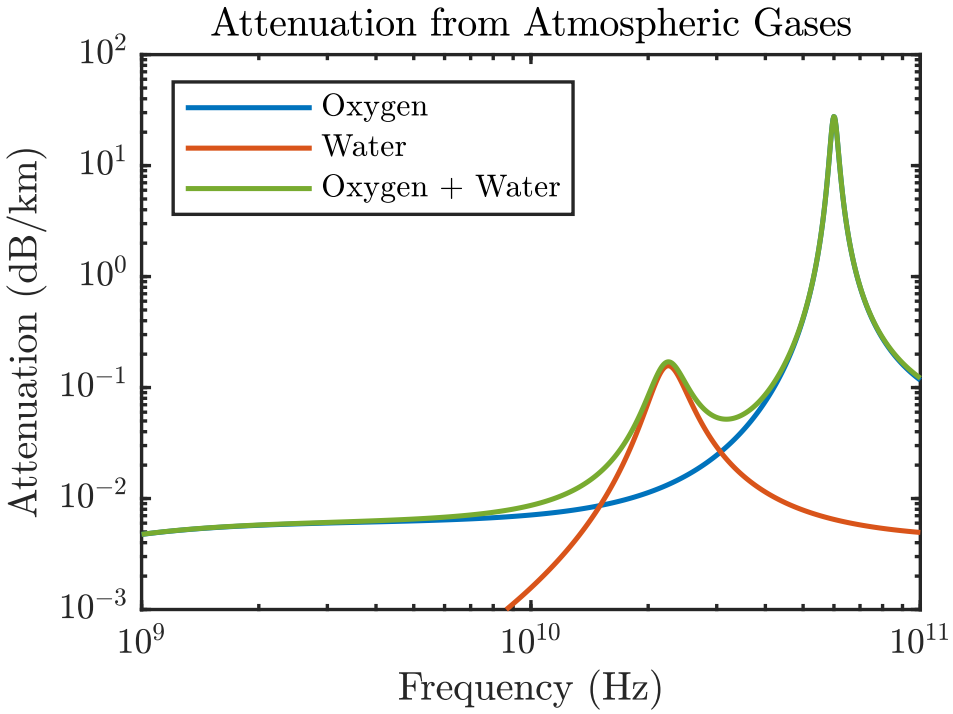

Figure 2.3: The total attenuation from atmospheric gases, given T=293K and ρ=7.

Table 2.1: Water concentration in different kinds of condensed, floating water collections. Types marked with * is from [2], the rest from [3].

	cloud*	ice cloud*	rad. and adv. fog	other fog
$\rho'[\mathrm{g/m^3}]$	1-2.5	0.1-0.5	0-0.1	0.1-1

Rain

The attenuation caused by rainfall is greatly dependent on rain rate and can be modelled by one-way attenuation [dB/km] $\alpha_{\text{rain}} = a \cdot rb$, with r being the rain rate [mm/hr] and a and b being constants dependant on drop-size, temperature, frequency and polarization [3, p.151].

Snow and hail

Because of how the refractive index of ice differs widely from that of water, the absorption and scattering from snow and hail differs from rain. This difference is accounted for using an equivalent rainfall rate $r_{\text{e}} = Xv$, with X being the mass concentration of snow [g/m^3] and v being the velocity of the snowfall [m/s]. The one-way attenuation [dB/km] then follows

$$\alpha_{\text{snow}} = 0.00349\frac{r_{\text{e}}^{1.6}}{\lambda^4} + 0.00224\frac{r_{\text{e}}}{\lambda} \tag{2.13}$$

showing an increase of attenuation with frequency [3, p.156].

Other attenuation

In addition to the previously mentioned, attenuation can also be caused by dust, smoke, insects and potentially other airborne particulates. These are however neglected here, given that they are difficult to predict from weather forecasts.

2.2 Meteorology and space weather

The atmosphere is a layer of gases between the Earth and space. Concerning meteorology there is no clear upper bound though some organisations (such as Fédération Aéronautique Internationale (FAI)) use the Kármán line at 100 km as the limit [10]. In reality all layers, bounds and -pauses in the atmosphere are approximate and fluid, with some of them changing with latitude, time-of-day and time-of-year. Throughout the whole atmosphere, air pressure decreases with height until finally merging with the vacuum of space.

2.2.1 Homosphere

The homosphere starts at sea-level and extends to 85km, when the concentration of particles has gone from roughly 10^{25}/m^3 to 10^{19}/m^3 [1, p.60]. Temperature can both increase and decrease with height and these regions are the basis for the atmosphere's lower layers.

Troposhere

The troposphere starts at the ground and reaches its end - the tropopause - at around 10km depending on at what latitude one measures (around 8km for the poles, 16km for the equator). Temperature is (in general) steadily decreasing with

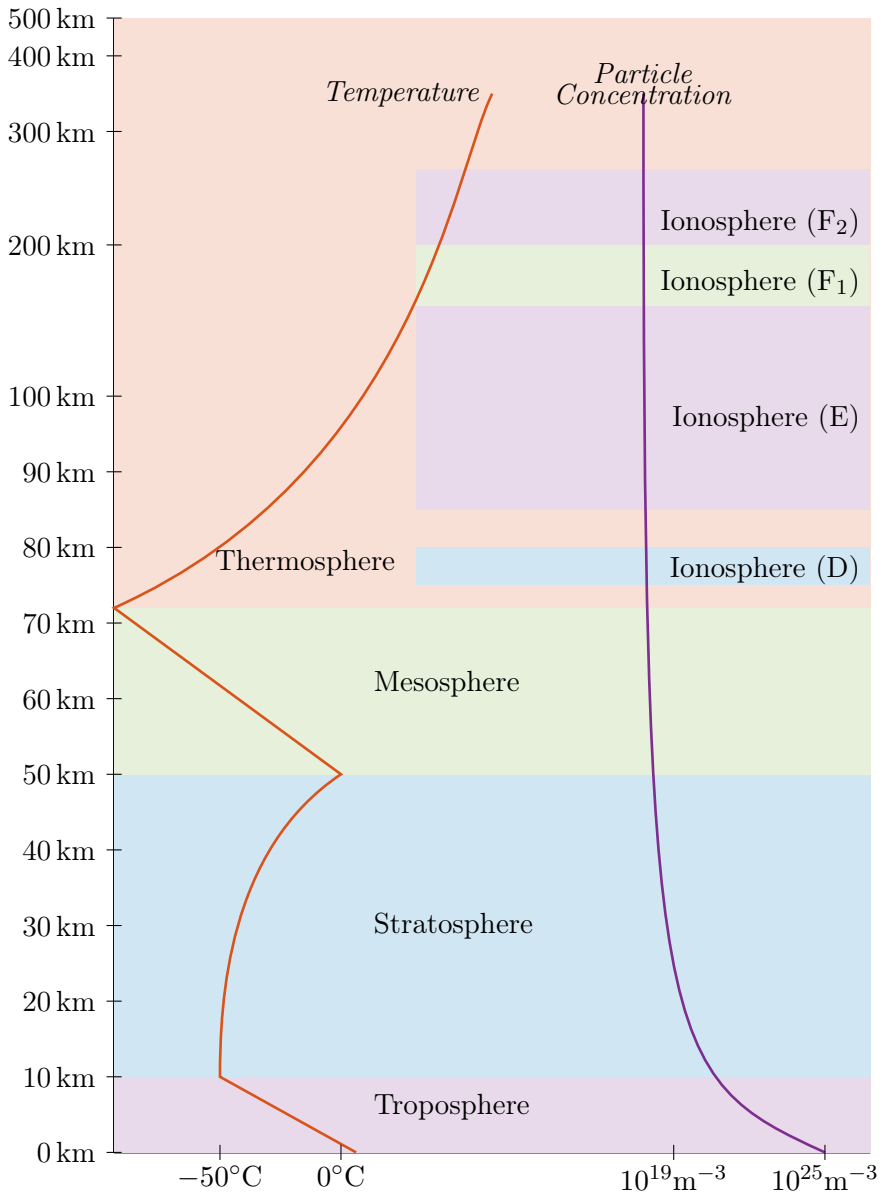

Figure 2.4: Schematic structure of the atmosphere and ionosphere. Heights are shown on a linear scale up to 100km and logarithmically compressed above. Temperature is plotted to the left and particle concentration to the right. Ionospheric heights from [1, p.65].

height throughout the troposphere, starting at around 10°C at ground-level to around −50°C at 10km. The troposphere contains roughly three quarters of all air in the atmosphere and 99% of its water vapour [1, p.59], with most of what we call "the weather" taking place here.

Stratosphere and Mesosphere

After the tropopause the stratosphere begins, continuing to around 50km. At its bottom, temperature is essentially constant but in the upper half temperature increases with height, stopping a bit below 0°C at the stratopause. This temperature increase comes from ozone (O_3) absorbing ultraviolet light, splitting into dioxygen (O_2) and oxygen (O) in an exothermic reaction [1, p.60]. Beginning at the stratopause, the mesosphere continues to around 85km above sea. As with the troposphere, temperature here is decreasing with height, to as low as −100°C at the mesopause.

These first layers all contain well mixed collection of gases — air — and it is this homogeneity that gives the collective name homosphere. It ends in the homopause, usually put at the same height as the mesopause, though they are defined differently; the mesopause is when temperature starts increasing with height, and the homopause is when turbulent mixing of gases end. Because of this it is also sometimes called the turbopause.

2.2.2 Heterosphere

The name heterosphere comes from the heterogeneity of the gases nitrogen, oxygen and hydrogen behaving separately. It consists of two subregions; the thermosphere and the ionosphere. Named from the fact that temperature is steadily increasing with height, the thermosphere refers to the non-ionized particles of the heterosphere.

Ionosphere

The ionosphere is the part of the heterosphere with ionized gases, and it is split into four layers; D, E, F_1 and F_2. All are present during the day but at night, when solar radiation is lower, the D-layer disappears and F_1 and F_2 combine into a single F-layer. All layers are made of charged particles; the D-layer consists of negative ions, the E-layer of positive molecular ions, the F_2-layer of positive atomic ions and the F_1-layer as a mixture of positive atomic and molecular ions [1, p.65]. Polarization of the layers does not affect reflection of RF waves. The refractive properties and more details on its effects of RF waves can be found in Section 2.3.2.

2.2.3 Anomalies

While the name implies rare events, anomalies are fairly common. The name instead refers to an atmospheric structure different from the one described above. The most common, and for us most important, anomaly takes place in the troposphere in the form of a temperature inversion. A temperature inversion in

the troposphere means that temperature increase with height instead of decrease. This leads to a stable layer in the atmosphere where hot, less dense air above cold, denser air have no incentive to mix [1, p.60]. This layer acts as a lid, keeping all air under it separate from the air above it. This can lead to moisture, smoke and the likes to accumulate causing phenomena like smog [11]. The trapping of moisture results in a steep moisture gradient which, as will be described in Section 2.3.4, results in large changes in refractivity. One cause of these inversions is called subsidence inversion where air in high pressure areas is pushed downwards. This leads to a temperature inversion where humidity decreases with height [12].

2.3 Refractive effects

No matter how clear the weather is, no one can see past the visual horizon. In the same way, no matter what the RRE says, no sensor can see past the radar horizon given a standard atmosphere. Ignoring the RRE for a minute, this section will cover how the horizon can shift for RF-based sensor systems.

Looking out along a body of water, the distance to the visual horizon can be calculated as shown in Figure 2.5. The Pythagorean theorem and the approximation that elevation is much smaller than Earth radius ($h \ll r$) gives

$$d_{\text{horizon}} = \sqrt{(r+h)^2 - r^2} = \sqrt{r^2 + 2hr + h^2 - r^2} \quad \left\{ h \ll r \right\} \Rightarrow d_{\text{horizon}} = \sqrt{2hr} \tag{2.14}$$

An often used approximation for calculating radar horizon is the effective Earth model, in which the same equation is used but with 4/3 Earth radius instead [2, p.57]. This puts the radar horizon slightly further away, as illustrated in Figure 2.6. What causes this shift in horizon is the refractive index of the atmosphere. Radar frequencies are more affected by the air than visual frequencies and as such, EM-waves in the RF spectrum are refracted more when propagating. In a standard atmosphere this causes a slight bend towards the Earth, resulting in a more distant horizon.

Though standard, a standard atmosphere is not overwhelmingly common and anomalies can lead to both a closer and more distant horizon. In order to get an accurate estimate of the radar range the effects of the current atmospheric events must be taken into account.

2.3.1 Atmospheric refractivity

For frequencies much smaller than 100 GHz ($f \ll 100$ GHz, and hence not applicable to visual wavelengths), refraction can be considered frequency independent as it is much more dependent on the parameters of the air itself [2, p.2]. Refractivity N is a scaled version of the more common unit refractive index, n. The scaling, $N = (n-1) \cdot 10^6$ and vice versa $n = N \cdot 10^{-6} + 1$, is used to get more manageable numbers; n in air generally fluctuates between 1.0002 to 1.0004, or 200 to 400 as N. The standard atmosphere mentioned in the previous section is defined as $N_{\text{standard}} = 310 - 0.039z$, with z indicating height in meters [13].

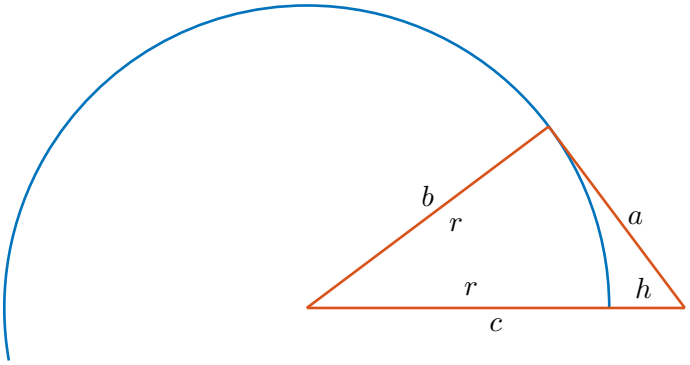

Figure 2.5: A right angled triangle inscribed in a circle (the Earth) can be used to calculate the visual horizon. Putting one corner of the triangle at the Earth's center, the other at the source and the last, the right angle, at the horizon, the length of hypotenuse c is radius plus elevation, the longer cathetus b is the radius and the shorter cathetus a is the distance to the visual horizon. a can be calculated from Pythagoras's theorem, $a^2 + b^2 = c^2$.

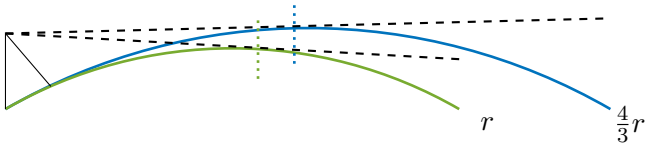

Figure 2.6: Using a larger radius when calculating distance to horizon moves the horizon slightly further away.

Atmospheric refractivity is calculated with

$$N = \frac{77.6}{T}\left(p + \frac{4810e}{T}\right) \tag{2.15}$$

which originates from a meta-study of many different experimentally found values [2, p.8]. The parameters responsible for refractivity N [-] is air pressure p [hPa], partial pressure of water vapor e [hPa] and temperature T [K].

Calculating the refractivity gradient of equation (2.15) and using the typical values $T = 280$ K, $e = 9$ hPa and $p = 1000$ hPa gives

$$\Delta N = 4.7\Delta e - 1.3\Delta T + 0.28\Delta p \tag{2.16}$$

which shows how the gradient of water vapour e is the main cause of anomalous propagation [14]. As stated in Section 2.2.3, these gradients can build from temperature inversions.

2.3.2 Ionospheric refractivity

The ionization of particles in the ionosphere causes a change in refractive index which affect EM-waves in a similar way as in the atmosphere. The refractive index in the ionosphere is dependent on both the frequency of the incoming radiation, as well as on the density of charged particles. A common approximation for the refractive index — which ignores polarization, diffraction from collisions with particles and the effects of the Earth's magnetic field [15] — is

$$n^2 = 1 - \frac{f_\mathrm{p}^2}{f^2}, \quad f_\mathrm{p}^2 = \frac{\rho e^2}{4\pi^2\epsilon_0 m} \tag{2.17}$$

with f_p being the so called plasma frequency. In this expression only electron density[4] ρ [m^{-3}] is a variable, as the other are constants. Using the values of the constants, equation (2.17) can be approximated to

$$\left.\begin{array}{ll} e = 1.6 \cdot 10^{-19}\mathrm{C} & \text{electron charge} \\ m = 9.1095 \cdot 10^{-31}\mathrm{kg} & \text{electron mass} \\ \epsilon_0 = 8.8542 \cdot 10^{-12}\mathrm{F/m} & \text{permittivity} \end{array}\right\} n^2 \approx 1 - \frac{80.1\rho}{f^2} \tag{2.18}$$

When n is imaginary, i.e. when f [s^{-1}] $\leq f_\rho = \sqrt{80.1\rho}$, a reflection is to be expected. This means that all waves, regardless of angle of incidence, will be reflected down to Earth. For $f > f_\rho$, the waves will not reflect but refract less and less until they, for $f \gg f_\rho$ simply pass through, barely affected by the ionosphere [16, p.286].

Values for ρ vary depending on time of day and solar activity, but typical values as well as what these correspond to in f_p are available in Table 2.2, where it is clear that only the F-layers are able to reflect waves from modern sensor systems. The limit is not set at 4 and 8 MHz though, as that is only the maximum frequency for reflection at normal incidence.

[4] Called N in sources, here called ρ to not mistake for refractivity N.

Table 2.2: f_ρ indicates the highest frequency to be reflected for a wave of normal incidence.

	D	E	F_1	F_2
Height [km]	75	100	150	200
N	10^9	$3 \cdot 10^9$	$2 \cdot 10^{11}$	$8 \cdot 10^{11}$
f_p	283 kHz	490 kHz	4 MHz	8 MHz

In order to calculate reflection from angles not of normal incidence, Snell's law (see Section 2.1.2) can be used, written as

$$n_a \cos\theta_\mathrm{a} = n_i \cos\theta_\mathrm{i} \tag{2.19}$$

with $_\mathrm{a}$ denoting atmosphere and $_\mathrm{i}$ ionosphere. Setting $n_\mathrm{a} \approx 1$ and n_i according to equation (2.18) gives

$$\cos\theta_\mathrm{a} = \sqrt{1 - \frac{f_\rho^2}{f^2}} \cos\theta_\mathrm{i} \Leftrightarrow \cos\theta_\mathrm{i} = \frac{\cos\theta_\mathrm{a}}{\sqrt{1 - \frac{f_\rho^2}{f^2}}} \tag{2.20}$$

A reflection occurs when $\cos\theta_\mathrm{i}$ is larger than allowed, i.e. $\cos\theta_\mathrm{i} \geq 1$. This gives

$$1 - \frac{f_\rho^2}{f^2} \leq \cos^2\theta_\mathrm{a} \Leftrightarrow 1 \leq \frac{f_\rho^2}{f^2} + \cos^2\theta_\mathrm{a} \tag{2.21}$$

Comparing this to the trigonometric identity $1 = \sin^2\alpha + \cos^2\alpha$ shows that

$$1 \leq \frac{f_\rho^2}{f^2} + \cos^2\theta_\mathrm{a} \Leftrightarrow f^2 \leq \frac{f_\rho^2}{\sin^2\theta_\mathrm{a}} \tag{2.22}$$

or that a wave with frequency f can be reflected as long as f is smaller or equal to $f_\rho / \sin\theta_a$, where θ_a is the grazing angle to the horizon [16, p.287]. As an example, $f = 16$MHz could be reflected from the F_2-layer for angles smaller than 30°.

This shows that given the right time of day (to get a large enough electron density ρ) and a flat enough angle of attack, EM-waves in above the MHz range can be reflected of the ionosphere.

2.3.3 Modified refractivity

Using refractive index n to calculate propagation is only accurate for short distances as the curvature of the Earth soon diverges from the rays [2, eq. 1.33]. Assuming that n varies in the vertical direction, and considering it constant for a certain Δz, one can view the atmosphere as many layers stacked on top of each other, with a shared middle at the center if the Earth. This opens up to using Snell's law for polar coordinates (see Section 2.1.2) in order to calculate the propagation of EM-waves along the ground. This however would force the use of polar coordinates throughout, making simulation and use of weather data much more

difficult. To avoid this, exchange n_x for $m_x \equiv n_x(1 + z/a)$, z[m] being height and a[m] being the Earth radius, resulting in

$$\begin{aligned} n_1 r_1 \cos\theta_1 = n_2 r_2 \cos\theta_2 \rightarrow &\left\{ m_x \equiv n_x\left(1 + \frac{z_x}{a}\right), \quad r_x = z_x + a \right\} \\ \Rightarrow m_1\left(1 + \frac{z_2}{a}\right)(z_1 + a)\cos\theta_1 &= m_2\left(1 + \frac{z_1}{a}\right)(z_2 + a)\cos\theta_2 \\ \Rightarrow m_1\left(z_1 + a + \frac{z_1 z_2}{a} + z_2\right)\cos\theta_1 &= m_2\left(z_2 + a + \frac{z_2 z_1}{a} + z_1\right)\cos\theta_2 \\ \Rightarrow m_1\cos\theta_1 &= m_2\cos\theta_2 \end{aligned} \quad (2.23)$$

which shows that the substitution $m = n(1 + z/a)$ allows use of Snell's law for flat surfaces, i.e. by using m instead of n when propagating an EM-wave, the surface of the Earth can be considered flat.

Since $z \ll a$, a commonly used approximation is $m \approx n + z/a$ [12, eq. (2)]. Using the same scaling mentioned in Section 2.3.1, we get the modified refractivity $M = (m - 1) \cdot 10^6$. Then, using N and M instead of n and m, the relationship $m \approx n + z/a$ can be further approximated (and defined) to

$$M \equiv N + 0.157z \quad (2.24)$$

given an Earth radius of $6.37 \cdot 10^6$ meters and z being expressed in meters [17, p.9]. This is the definition used when modifying the refractivity.

2.3.4 Anomalous propagation

As a result of the refractive index gradient caused by atmospheric anomalies, anomalous propagation of EM-waves can take place. The propagation types are classified as either super deflection[5], standard, sub deflection, or ducting. Illustrated in Figure 2.7, these phenomena either bend the waves away from the Earth, along the effective Earth model, slightly more towards the Earth, or trapping them entirely.

All of these propagation versions greatly affect the range of a sensor system, though ducting is the one most commonly described and sought after. Ducts are differentiated depending on at what height they appear, with further categories based on their cause [18]. Modified refractivity M is the most commonly used metric for visualising these ducts, where an M-profile increase by ~ 118 per kilometre corresponds to a standard atmosphere [19], i.e. the effective Earth model. Ducts may appear when $\partial M/\partial z \leq 0$, and this region is called a trapping layer. Following are the different kinds of ducts, with illustrations in Figure 2.8. A description on how read these diagrams can be found in the appendix, Section A.1

[5]Some sources use the word "refraction" instead of "deflection". Both versions occur with the prefixes "super" and "sub" to indicate the same phenomena. It seems to be a matter of taste and given the context of propagation, not refractive index, I have opted to use "deflection".

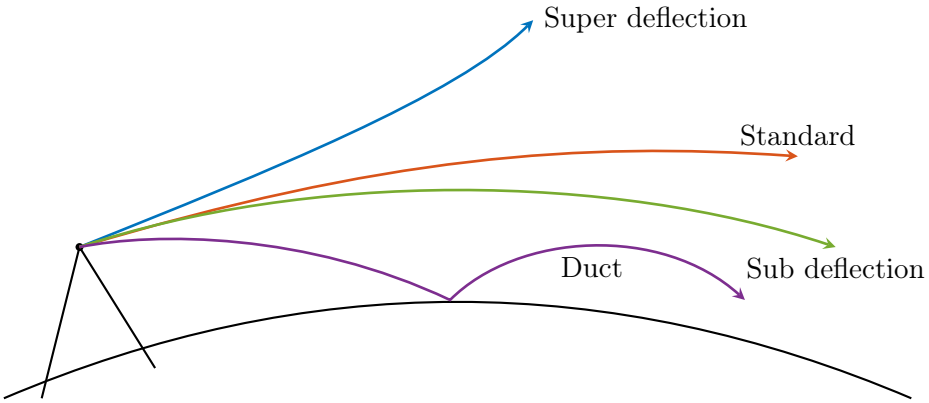

Figure 2.7: Illustration of the different propagation anomalies.

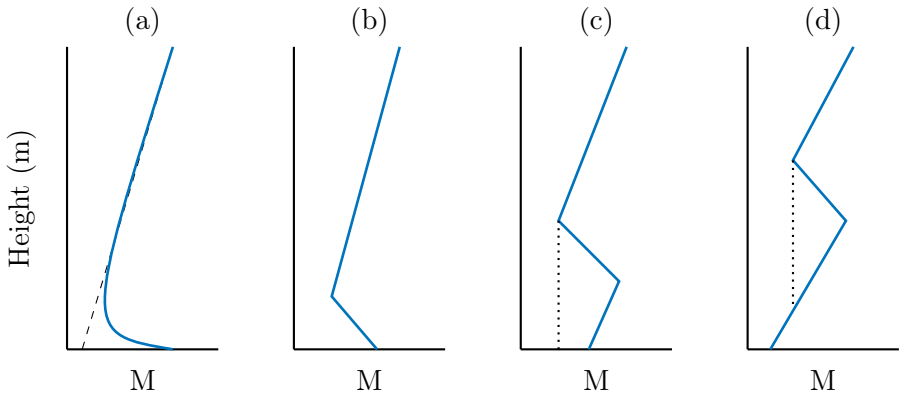

Figure 2.8: (a); a dashed standard profile along with an evaporation duct, with its low and sharp trapping layer. (b); an ordinary surface duct and (c); a surface-based duct, both requiring a reflective surface below for ducting. Finally (d); an elevated duct.

Surface ducts

Surface ducts are defined as when the bottom of a trapping layer connects to the ground. This can be caused by either evaporation or advection. Evaporations ducts are in general very thin (5-6m in Nordic waters while around 20m in the Persian Gulf [18]) and cover large areas ($\sim$ 1000km) above water. Advection ducts appear a bit higher up (40-200m) and in coastal areas, as they are caused by warm and dry inland air creeping out (advecting) over the adjacent, colder waters [12]. This can be fairly common during the summer, and especially at dusk.

Surface-based ducts

If the trapping layer has its local refractivity maximum above the ground, as well as its minimum being smaller than the ground value, a surface-based duct is formed. They appear from similar phenomena as surface ducts and behave in the same way. For both duct types, EM-waves are bent downwards by the refractive index gradient, and reflected back up by the surface of the water.

Elevated ducts

If the smallest value of the refractivity of the trapping layer is larger than the value at the ground, an elevated duct is created. These ducts are often caused by subsidence inversions, which can span areas of 500-1000km and exist for weeks at a time. Propagation in elevated ducts do not require a reflected surface, as the lower part is usually large enough to bend the EM-waves back up [18].

2.4 Weather data

During the work of this thesis, many different data sources have been considered and tried. In Table 2.3 below the sources are listed, as well as what relevant data they contain and in what units. It is worth noting that measurements from 1995 show that meteorological data needs a fidelity of 7 meters vertically and 15 km horizontally in order to properly predict propagation [12].

2.4.1 Data format

General Regularly-distributed Information in Binary (GRIB) is a data standard introduced in 1994 by the World Meteorological Organization (WMO). The current version, GRIB2, was released in 2003. Each .GRIB file contains a header describing the data, as well as the data itself. Each data point is spaced out on a regularly spaced grid, oriented along latitude and longitude. Each one of these data grids are indexed in the header as Band, where one data type (for example temperature) can occupy one band for each height level. Both Swedish Meteorological and Hydrological Institute (SMHI) and European Centre for Medium-Range Weather Forecasts (ECMWF) uses GRIB to export their data sets.

Table 2.3: Meteorological variables available from different weather data sources.

	MEPS	AROME	ERA5	CERRA
Organisation	SMHI	SMHI	ECMWF	ECMWF
Geo. region	Nordics	Nordics	Europe	Europe
Temperature	°C	K	°C	°C
Pressure	Pa	Pa	Pa[(a)]	Pa
Humidity	kg/kg[(b)]	kg/kg[(b)]& %[(c)]	kg/kg[(b)]	%[(c)]
Height	hybrid levels	$m^2/s^{2(d)}$	$m^2/s^{2(d)}$	[(e)]
Precipitation	type, $kg/m^{2(f)}$	$kg/m^{2(f)}$	–	–

[(a)]for surface pressure. For higher levels one consults an array, listing pressure in [hPa]
[(b)]Specific humidity
[(c)]Relative humidity
[(d)]Geo-potential
[(e)]One model present values at specific hx meters above a base pressure, one model uses hybrid levels
[(f)]For rain, snow, graupel and total

2.4.2 Hybrid Level

As pressure is mostly independent of other weather factors, hybrid levels are used in some meteorological data as an alternative to presenting pressure at multiple heights. Instead, pressure is presented at ground level, with tables available to calculate pressure at the other levels. It starts from hybrid level 1 as the highest[6] level down to the lowest. As mentioned in Section 2.4.1, these levels then exist for other data as well, such as temperature and humidity.

For SMHI Meteorological Ensemble Prognosis System (MEPS)-data there are 65 hybrid levels, as well as the surface pressure p_s. Pressure at the hybrid levels is calculated from

$$p_{lev} = a_{full} + b_{full} \cdot p_s \tag{2.25}$$

where a_{full} and b_{full} are the linearly interpolated values from tables a_{half} and b_{half} (see Table 2.4) [20]. Both half-tables contain 66 values, giving 65 values to the full-tables.

From the pressure difference between levels, geometric height can be calculated using the approximation that every 1 hPa pressure difference is 8 meters height difference.

[6]Elevation-wise. Notice that pressure decrease with height, so high pressure is indicative of a low elevation.

Table 2.4: a_{half} and b_{half} values for MEPS. Read from left to right, then top to bottom for each value.

a_{half}		b_{half}	
1-65	2-66	1-65	2-66
0.00000000	2000.00000000	0.00000000	0.00000000
4000.21287319	6002.09662113	0.00000000	0.00000000
7911.25838577	9633.01049417	0.00095468	0.00382570
11169.37146237	12522.57753978	0.00862327	0.01535782
13695.00149653	14689.11546998	0.02404046	0.03468314
15507.49052823	16154.69697732	0.04729839	0.06195102
16632.12471208	16940.14949960	0.07868187	0.09744325
17082.34869816	17065.28164099	0.11815586	0.14071098
16898.18367797	16592.58939571	0.16497348	0.19078554
16161.90395878	15620.94340550	0.21797086	0.24633925
14985.46502362	14271.70773051	0.27569119	0.30582244
13495.95994372	12674.16909910	0.33652825	0.36760726
11821.60314859	10952.57042620	0.39886479	0.43011564
10080.20053763	9216.28565403	0.46118624	0.49191624
8371.17893039	7553.74479607	0.52215946	0.55178443
6771.35457397	6029.92021691	0.58067442	0.60872709
5333.95880836	4686.68074804	0.63585388	0.66197911
4090.09511346	3545.12645110	0.68703898	0.71098036
3051.73811264	2609.05813936	0.73375964	0.75534143
2215.50455766	1868.90774223	0.77569737	0.79480486
1566.62821060	1305.66882073	0.81264598	0.82920633
1081.85503306	890.47596795	0.84454000	0.85875505
727.74548529	590.17748096	0.87191802	0.88409276
474.58767980	378.08857614	0.89534045	0.90571965
298.07947335	232.23312781	0.91528643	0.92409452
178.48015386	134.99207440	0.93219549	0.93963895
100.16369201	72.59529482	0.94647277	0.95274328
51.07508967	34.56216490	0.95849551	0.96377340
22.17022046	13.15225964	0.96862008	0.97307803
6.88641310	2.86306141	0.97718944	0.98099640
0.67344356	0.00000000	0.98454132	0.98786727
0.00000000	0.00000000	0.99102462	0.99406510
0.00000000	0.00000000	0.99703923	1.00000000

Chapter 3

Split-Step Parabolic Equation

The Split-Step Parabolic Equation (SSPE) is a popular method for simulating EM-wave propagation through variable refractivity and terrain. It was first proposed in 1988 by Dockery [21], inspired by previous work with acoustic waves by Tappert in 1973 [22]. Since then it has been improved by Dockery [23] and used by numerous others [24], [12].

3.1 Parabolic approximation of Maxwell's equations

The Parabolic Equation (PE) is an approximation of the wave equation. By using equations (2.1) and (2.4) from Section 2.1.1 and modifying for no sources, one can derive the wave equation

$$\nabla^2 \mathbf{E} = \mu_0 \epsilon_0 \frac{\partial^2 \mathbf{E}}{\partial t^2} \tag{3.1}$$

From here an assumption of $\mathbf{E}(\mathbf{r}, t) = \mathcal{R}\big[\mathbf{E}(\mathbf{r})e^{-i\omega t}\big]$ is made. Assuming propagation through non-vacuum also necessitates changing ϵ_0 and μ_0 to $\epsilon = \epsilon_0\epsilon_\mathrm{r}$ and $\mu = \mu_0\mu_\mathrm{r}$. Remembering that $n = \sqrt{\mu_\mathrm{r}\epsilon_\mathrm{r}}$ and that $c = \sqrt{\mu_0\epsilon_0}^{-1}$ results in

$$\nabla^2 \mathbf{E} + k^2 n^2 \mathbf{E} = 0, \quad k = \frac{\omega}{c} = \frac{2\pi}{\lambda} \tag{3.2}$$

Propagation is then chosen to be in a Cartesian system with height in $\hat{z}$, distance in $\hat{x}$ and no propagation in $\hat{y}$,

$$\partial_x^2 \mathbf{E} + \partial_z^2 \mathbf{E} + k^2 n^2 \mathbf{E} = 0 \tag{3.3}$$

which rewritten with $u(x, z) = \mathbf{E}(x, z)e^{-ikx}$ for propagation along $\hat{x}$ ends up as

$$\Big[\partial_x^2 + 2ik\partial_x + \partial_z^2 + k^2(n^2 - 1)\Big]u(x, z) = 0 \tag{3.4}$$

We can then split equation (3.4) into one forward and one backward propagating part by splitting operator ∂_x into two pseudo-differential operators[1]. This is done

[1] A pseudo-differential operator is a differential operator which is defined in the Fourier domain only.

by initially rewriting equation (3.4) as

$$\begin{aligned}\Big[\partial_x^2 + 2ik\partial_x + \partial_z^2 + k^2(n^2-1)\Big]u(x,z) &= 0\\ \Big(\partial_x^2 + 2ik\partial_x - k^2\Big)u(x,z) + \Big(\partial_z^2 + k^2n^2\Big)u(x,z) &= 0\\ \Big(\partial_x + ik\Big)^2 u(x,z) + \Big(\partial_z^2 + k^2n^2\Big)u(x,z) &= 0 \qquad (3.5)\end{aligned}$$

Introducing the Fourier transform,

$$\hat{u}(x,p) = \mathcal{F}[u(x,z)] \equiv \int_{-\infty}^{\infty} u(x,z)e^{-ipz}dz \qquad (3.6)$$

to transform (3.5) along $\hat{z}$ into (ignoring vertical changes in n)

$$\Big(\partial_x + ik\Big)^2 \hat{u}(x,p) + \Big(k^2n^2 - p^2\Big)\hat{u}(x,p) = 0 \qquad (3.7)$$

accepting that the Fourier transform of operator ∂_z is ip and consequently that $\mathcal{F}(\partial_z^2) = -p^2$, in accordance to [25]. Equation (3.7) can then be isolated as a pseudo-differential operator on the form

$$\begin{aligned}\Big(\partial_x + ik\Big)^2 &= -\Big(k^2n^2 - p^2\Big)\\ \partial_x + ik &= \pm i\sqrt{k^2n^2 - p^2}\\ \partial_x + ik &= \pm ik\sqrt{n^2 - p^2/k^2}\\ \partial_x &= -ik\Big(1 \mp \sqrt{n^2 - p^2k^{-2}}\Big) \qquad (3.8)\end{aligned}$$

Inverse Fourier transforming this, again with $\partial_z^2 \leftrightarrow -p^2$, and with $Q = \sqrt{k^{-2}\partial_z^2 + n^2}$, where the action of Q on a function u is defined as $Qu = \mathcal{F}^{-1}\big(\sqrt{n^2 - p^2k^{-2}}\hat{u}\big)$, gives [24]

$$\partial_x u = \begin{cases} -ik(1-Q)u & \text{forward} \\ -ik(1+Q)u & \text{backward} \end{cases} \qquad (3.9)$$

Rewriting Q_{forward} according to [26],

$$Q = \sqrt{\frac{1}{k^2}\partial_z^2 + n^2} \Leftrightarrow \sqrt{1+A+B} \quad \begin{cases} A = & \frac{1}{k^2}\partial_z^2 \\ B = & n^2 - 1 \end{cases} \qquad (3.10)$$

approximating

$$\sqrt{1+A+B} \approx \sqrt{1+A} + \sqrt{1+B} - 1 \qquad (3.11)$$

and using the identity $\sqrt{1+A} = 1 + A(\sqrt{1+A}+1)^{-1}$ lets us rewrite the forward part of equation (3.9) as

$$\partial_x u = \left(\frac{i\partial_z^2}{\sqrt{k^2 + \partial_z^2} + k} + ik(n-1)\right)u \qquad (3.12)$$

which can be used to step the solution forward in x.

3.2 Split-step

Equation (3.12) shows a first order derivative in $\hat{x}$ and second order derivatives in $\hat{z}$. In order to solve this a split-step approach is taken, meaning that $u(x, z)$ is advanced by a step Δx to $u(x + \Delta x, z)$. In each of these steps, the equation is Fourier transformed from z to p using the appropriate transform equation (3.6), with $p = k \sin\theta$ and θ being the angle from the horizon. Given an n that is locally constant in both x and z, the Fourier transform has a simple solution at $x + \Delta x$ based on the solution at x [21]. This can be done efficiently using a fast Fourier transform (FFT).

Looking at equation (3.12) and considering the step from $u(x, z)$ to $u(x+\Delta x, z)$ for a small Δx, this equation is reformulated as

$$u(x + \Delta x, z) = e^{\frac{i\partial_z^2 \Delta x}{\sqrt{k^2+\partial_z^2}+k}} \cdot e^{ik(n-1)\Delta x} u(x, z) \tag{3.13}$$

Fourier-transforming all of this along $\hat{z}$ gives

$$u(x + \Delta x, z) = e^{ik(n-1)\Delta x} \mathcal{F}^{-1} \left\{ e^{-ip^2 \Delta x \left(\sqrt{k^2-p^2}+k \right)^{-1}} \cdot \mathcal{F} u(x, z) \right\} \tag{3.14}$$

which is the basis for the propagation algorithm.

3.2.1 Step size

For both x and z, the step size is important for correct results. For z, the limiting factor is the angle of propagation and aliasing effects. After choosing a maximum height, $z_{\max}$, $p_{\max}$ is set according to the Nyquist criterion $p_{\max} \cdot z_{\max} = \pi N$, N being the total amount of steps along $\hat{z}$. At the same time, $p_{\max} = k \sin\theta_{\max}$. All of this together gives

$$\Delta z = \frac{z_{\max}}{N} = \frac{\pi}{p_{\max}} = \frac{\pi}{k \sin\theta_{\max}} = \frac{\lambda}{2 \sin\theta_{\max}} \leq \frac{\lambda}{2 \sin\theta} \tag{3.15}$$

meaning that the step-size Δz must be smaller than $\lambda / \big(2 \sin\theta\big)$[24]. What θ should be depends on the situation, but it can be fairly small as propagation rarely diverge beyond a few degrees from horizontal.

Discretization along $\hat{x}$ is more unclear. The split-step approach is stable as long as n is locally constant, which can be true if Δx is small compared to horizontal changes in n. Despite this Δx can still be large compared to wavelength [21]. In practice, Δx is most easily set by trial and error, lowering Δx until results start converging.

Chapter 4
Simulation software

4.1 Reasoning behind choice of method

Many different methods for simulating EM-waves exist, but this thesis has chosen to focus on and use the wide angle SSPE. Following is the reasoning behind this choice.

In the 70's Ray Tracing (RT) was popular, as it was not too computationally demanding for computers at the time. It however lacked some factors of importance, such as interference patterns from multi-path propagation.

This is addressed when using the parabolic equation to simulate the waves, though there are restrictions on too wide propagation angles. These restrictions however are mostly a problem when dealing with reflections, as most sensor systems are designed to have a very narrow beam. Some thought could be put towards passive sensors, where it is possible that the source is not narrow and therefore cause interference by multipath propagation.

The PE used in this thesis uses the Wide Angle approximation (WAPE). This is in contrast to the Narrow Angle approximation (NAPE) which instead of the approximation in equation (3.10) sets $Q = \sqrt{1+q}$, $q = k^{-2}\partial_z^2 + n^2 + 1$ and approximates that according to the first order Taylor expansion, $Q \approx 1 + q/2$. Both the NAPE and the WAPE are implemented in the same way and require the same amount of equations, but the WAPE can handle larger propagation angles and introduces less errors [26]. [26] uses Strang splitting when advancing from x to $x + \Delta x$, but this did only seem to affect results while slow calculations down, and is not present in later sources such as [24].

Another problem with the parabolic equation are boundary conditions. The Discrete Mixed Fourier Transform (DMFT) [23] solves each boundary at each step, but this adds eight computations for each range-step, leading to increased computation time. Using the SSPE instead, boundaries can be handled by changing refractive index or by applying a window function, though this is not necessarily based on correct physics.

The most complete simulation procedure is the Finite Element Method (FEM). While allowing for far more freedom regarding irregularities and boundaries, it is extremely computationally demanding and difficult to implement.

As a compromise between accuracy, ease of implementation and computational time, the wide-angle SSPE has been chosen.

4.2 Data

Meteorological data is imported from SMHIs prognosis model MEPS [27] which contains numerous parameters for 65 different levels. As stated in Section 2.3.1, atmospheric refraction is dependent on temperature, humidity and pressure, all of which are included in MEPS. In addition to this, data of cloud coverage and whether the ground is land or sea is imported. Precipitation data consisting of rain rate and precipitation type is also imported.

4.2.1 Reading of data

Installing the MATLAB Mapping Toolbox, the imported GRIB-file is read using `readGeoRaster()` which is capable of reading GRIB since MATLAB R2023b. Entries are numbered but can most easily be found by searching for their element name.

For all height levels (1-HYBL to 65-HYBL), the bands TMP (temperature), SPFH (specific humidity) and 466:530 (cloud coverage, not readable by phrase) are read and saved to separate $949 \times 1069 \times 65$ matrices. In addition to this single-level parameters are also read. These are PRES (pressure), 548 (specific humidity 2 m above ground), 546 (temperature 2 m above ground), PTYPE (type of precipitation), RPRATE (rate of precipitation) and 3 (ground type). Both ground level data and 2 m data are treated as ground level.

Pressure at all levels is calculated from the surface pressure according to Section 2.4.2. The ground level/2 m-data is added as an additional lowest height level (index 66). From then on, height [m] for each level is calculated from

$$\text{geoHeight} = (\text{lowPoint} - \text{levelPres}) \cdot 0.08 \tag{4.1}$$

with lowPoint being the highest pressure [Pa] on the map and geoHeight and levelPres being height and pressure for the different levels, respectivly.

Exported from this are four $949 \times 1069 \times 66$ matrices containing temperature, specific humidity, pressure and geometric height. An additional $949 \times 1069 \times 68$ matrix showing cloud coverage for 1:65, and precipitation type, ground type and precipitation rate for 66:68 is also exported. The 949×1069 dimensions of these matrices span the Scandinavian peninsula, with each entry spaced 2.5 km apart in both directions. The refractivity is calculated from these matrices and equation (2.15).

4.2.2 Handling of data

As a first step in creating the refractivity slice, the user gets to input coordinates[1] of the start and end of a line, as well as a desired maximum height. The function `griddedInterpolant()` is used to interpolate values along the chosen line. Returned is a 2D matrix representing a vertical slice of the original data. This slice is then for-looped along its horizontal range, where each step is moved to the correct geometric height and interpolated according to the chosen height range.

[1] As of now, these are simply in a (x,y) format but could be changed to (Lat,Long) in the future.

Exported from this part of the code is the refractivity slice, attenuation slice and ground information, as well as arrays for both vertical och horizontal range. A for-loop is then used to modify the slice to modified refractivity, adding 0.157 for every meter of elevation (in accordance to equation (2.24)).

4.3 Simulation

The simulation was done using the wide angle SSPE described in Section 3. The refractivity values of the slice are scaled to refractive index, which is then entered into the SSPE along with wavelength, vertical and horizontal range, ground type, antenna height, tilt and beamwidth, and the attenuation slice. Though part of the theory, ionospheric refraction is not included as the height required is much larger than feasible to simulate. The low frequencies ($\lesssim 1$ GHz) required are also deemed non-interesting for this thesis. As the initial field u_0, attenuation, window function and boundaries are subject to taste these will be described below. Step size and implementation of $p = k \sin\theta$ is also described.

4.3.1 Step sizes

According to Section 3.2.1, the upper bound for Δz is $\lambda/(2\sin(\theta_{\max}))$. By trying different values for maximum propagation angle $\theta_{\max}$ it was found that

$$\theta_{\max} = \big(|\text{tilt}| + |\text{beamwidth}|\big) \cdot 1.2 \tag{4.2}$$

makes the simulation converge while keeping Δz as large as possible. For very rough terrain where reflections from the ground can exceed $\theta_{\max}$, the angle of those reflections should be used instead of tilt and beamwidth[2].

Since Δx is limited only by keeping n locally constant, the maximum gradient horizontally was found for the chosen slice, and through trial and error $\Delta x = 250/\text{gradient}_{\max}$ was chosen as an appropriate discretization.

For both of these discretizations, the goal was to keep them as large as possible in order to minimize computation time. By only having Δz dependent on wavelength λ, increase in time from increased frequency follows the complexity of the FFT, $\mathcal{O}(N \log N)$.

4.3.2 Building $p = k \sin\theta$

Numerically, $p = k\sin\theta$ is made as $p = 2\pi\big[0 : (N_z/2-1), (-N_z/2) : -1\big]/\big(N_z \cdot \Delta z\big)$, with N_z being the number of steps in $\hat{z}$ and Δz being the step length. This is the correct discretization for even Fourier transforms, and when the data is interpolated into slices, care is taken that N_z is always even.

[2]The beamwidth is described in degrees from horizontal

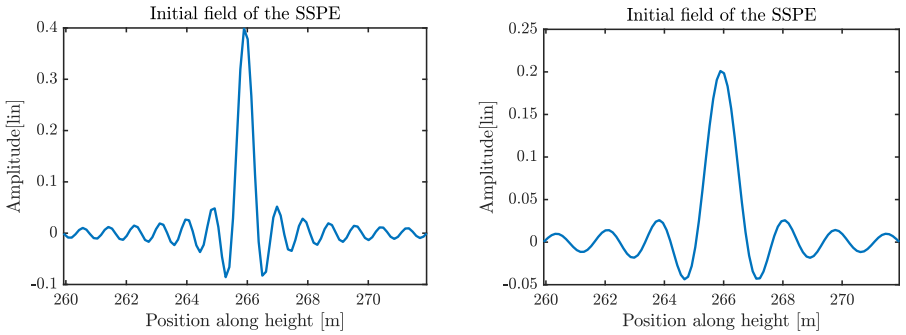

(a) Beamwidth 2°, tilt 0° **(b)** Beamwidth 1°, tilt 10°

Figure 4.1: The initial field as generated from a source of 10GHz, 200 meters above ground (266 above local zero). Beamwidth and tilt expressed in degrees.

4.3.3 Initial field

In order to model a general EM source, the initial field u_0 is set according to

$$u_0 = \frac{\sqrt{\lambda}}{\pi \cdot (z - z_0)} \cdot \sin \frac{2\pi \cdot (z - z_0) \cdot \tan \vartheta}{\lambda} \cdot \frac{I_0(\alpha \cdot \beta)}{I_0(\alpha)} \tag{4.3}$$

as seen in Figure 4.1, with ϑ being the half-width of the source aperture and I_0 being the modified Bessel function. The factor α is set to 4.2978 and $\beta = \sqrt{1 - [(z - z_0)/(z_{\max} - z_0)]^2}$, all in accordance to [26]. This field is further modified by

$$u_0 \cdot e^{-ik_0 \sin(\text{tilt})\text{z}} \tag{4.4}$$

in order to tilt the antenna up or down.

4.3.4 Attenuation

Attenuation α has the same dimensions as the refractivity slice. For each attenuation type presented in Section 2.1.6, that typed value is calculated and added to to total attenuation. For cloud or fog, the ρ' coefficient is set to 1 for all points above 200 m and 0.1 for all under. This is a very crude way of assuming water density based on height; clouds are said to be above 200 m and fog to be under 200 m. As the resulting value is the one-way dB/km, it is divided by 1000 before being used in the SSPE (to convert to [dB/m]). It is then multiplied to the field $u(x, z)$ as propagation factor $F = 10^{-0.1\alpha \cdot dx}$.

4.3.5 Window function and boundaries

Since the Fourier transform is periodic, propagation leaving the top of the slice will appear at the bottom, and vice versa. This is non-physical and needs to be addressed with well chosen boundaries.

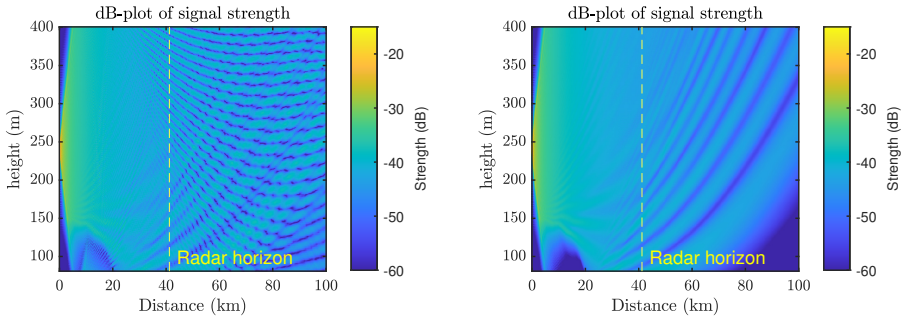

(a) An abrupt change from 1 to 0

(b) A gradual change from 1 to 0

Figure 4.2: Notice the feather-like pattern caused by constructive interference from reflections against the top and bottom, disappearing for the top when adding a taper. The dark blue bump to the left is ground.

At the top of the slice the goal is to attenuate the wave as if dispersing into space. Multiplying the field $u(x, z)$ with a window function, this window function can be set to 1 where propagation is wanted, and 0 where unwanted. An abrupt change in value will however cause reflections, see Figure 4.2a, so a Hanning taper,

$$w(i) = 0.5\left[1 - \cos\left(2\pi\frac{i}{I}\right)\right], \quad 0 \leq i \leq I \tag{4.5}$$

is used to ease the transition from 1 to 0. A long enough taper will attenuate almost all reflections[21], see Figure 4.2b.

While the reflections in Figure 4.2a appear from abrupt changes in the window function, similar reflections appear from changes in refractive index. By subtracting a small imaginary value from n, the wave is not only reflected but also attenuated, see Figure 4.3.

All of the sub-figures in Figure 4.3 show propagation through the same vertical slice but with different imaginary values added. Values larger than 10^{-3} do not make any noticeable difference, nor do values smaller than 10^{-5}. The land area is the bump to the left of the graphs, with water starting directly to the right of it.

There are more rigorous approaches for implementing reflections in both [24] and [21] but these are based on the conductivity and permittivity of the surface. Given that this data is subject to change based on type of ground, salinity of water etc., the current approach was deemed to be good enough for a rough estimate, though it would benefit from comparative measurements.

4.4 Visualizations and output

In order to understand the data the user is supplied with many graphs. These are supplied in steps, meant to be of use when choosing parameters for the next step. The yellow, dashed line “Radar horizon” in all propagation plots is based on the

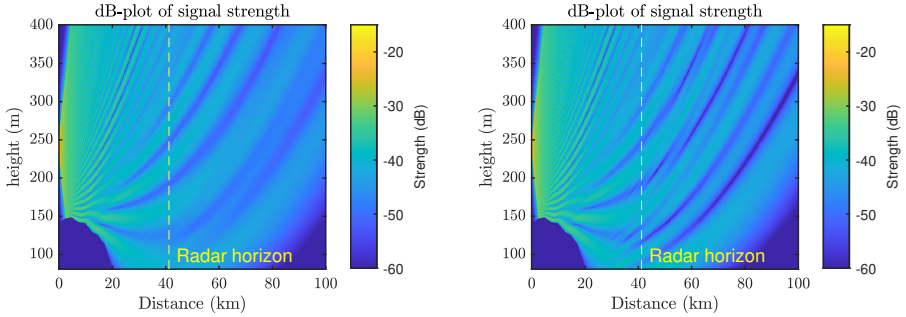

(a) Land $n + i \cdot 10^{-3}$, water $n + i \cdot 10^{-5}$

(b) Both $n + i \cdot 10^{-3}$

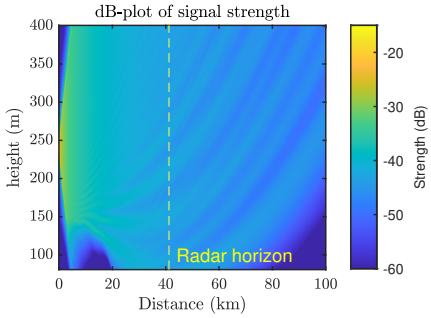

(c) Both $n + i \cdot 10^{-5}$

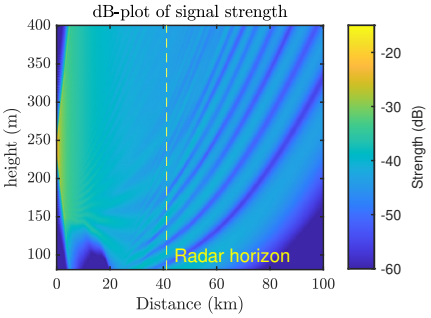

(d) Land $n + i \cdot 10^{-5}$, water $n + i \cdot 10^{-3}$

Figure 4.3: Four examples of how the imaginary value affects the wave. in a) and d) water and land are assigned different values, with d) being the realistic version. Notice the difference in clarity of the interference pattern.

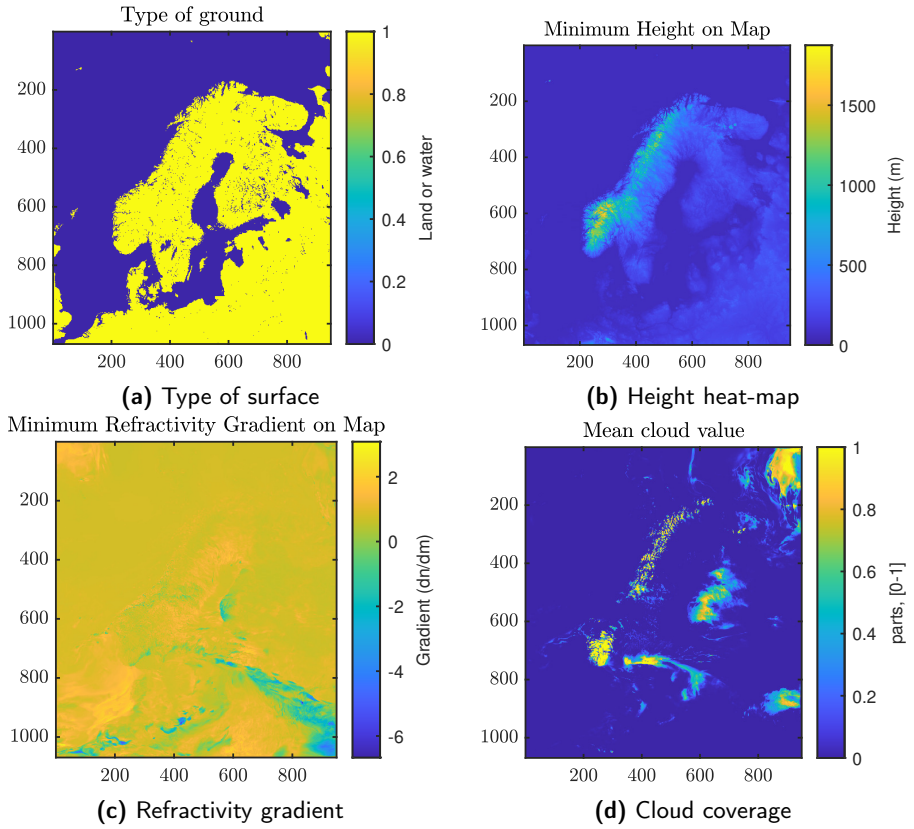

(a) Type of surface **(b)** Height heat-map

(c) Refractivity gradient **(d)** Cloud coverage

Figure 4.4: The four plots supplied to the user in an initial state, in order to get an overview of the current meteorological situation.

calculations presented in Section 2.3, with height corresponding to the source's elevation above the surface.

4.4.1 Before choosing slice

Initially, ground type (Figure 4.4a), ground height (Figure 4.4b), minimum refractivity gradient (Figure 4.4c) and cloud coverage (Figure 4.4d) are plotted. These help the user with orienting themself, and offer important information on what behaviour to expect. A low refractivity gradient indicates a higher change of ducts, a large cloud coverage could mean large attenuation, and large height differences could cause problems for the SSPE, as it works best for strictly horizontal propagation. These could be superfluous as the user probably has an area in mind from the start, but in that case they are easily skipped.

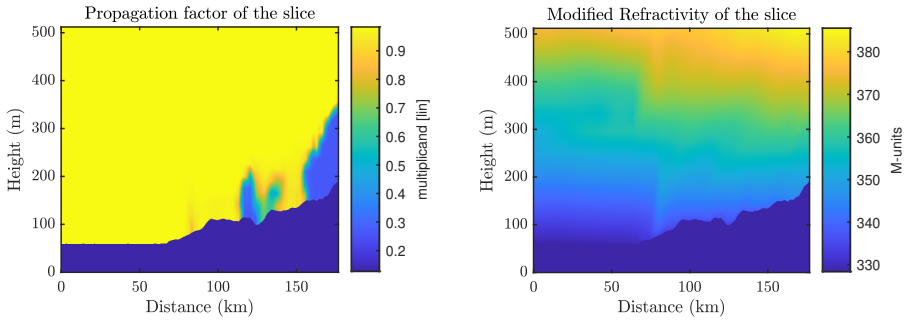

(a) Propagation factor F, $10^{-0.1\alpha \cdot dx}$ **(b)** Continuous Modified Refractivity

Figure 4.5: Propagation factor and refractivity for the chosen slice, in order to get a feel for the slice before simulation.

4.4.2 Before SSPE

From the previous plots, height and position of the slice can be chosen based on $x-$ and $y-$coordinates. Frequency is chosen now as well, in order to get the correct discretization along the slice. Looking at Figure 4.5, one can get a feel for how the wave will propagate. The propagation factor shows how much it will attenuate, and the modified refractivity can show interesting variations in the refractive index. Wanting a more traditional view of the refractive index, the user can turn to Figure 4.6. Differences from standard atmosphere are easily noticed here. A height map with the position of the slice overlaid is also here, as a method of double-checking position.

4.4.3 After SSPE

After simulation, a plot of the propagation is presented, Figure 4.7. What is plotted is a logarithmic value of u, $20\log(\text{abs}(u))$, where u beforehand has been normalized to the initial source, $u = u/\sqrt{\text{sum}(\text{abs}(\text{u0})^2)}$. This means that the total initial power is set to 1, and that the value on the colour bar is the change from 0 dB. The Radar horizon is plotted in order to show what range is expected and whether range has improved or not.

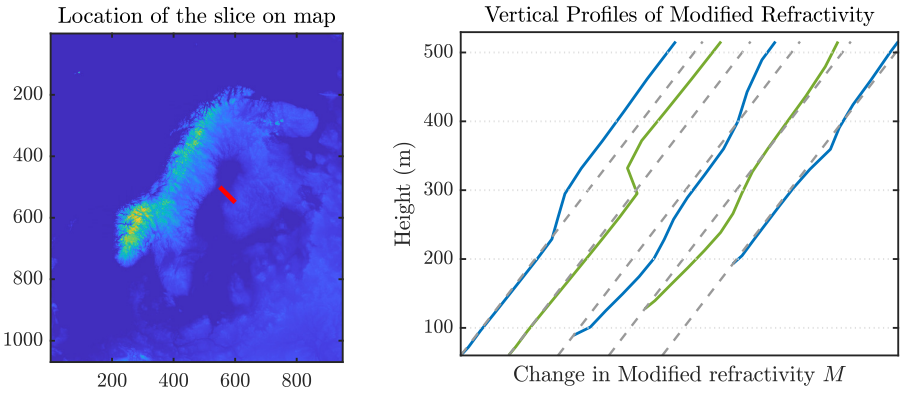

(a) Location of the slice on map

(b) M-diagram along the slice

Figure 4.6: Location of the slice and a more traditional M-diagram, with M-values evenly spaced along the slice. For reference, the dashed lines show a standard atmosphere. Since deflection is dependent on $\partial M/\partial z$, absolute values are omitted.

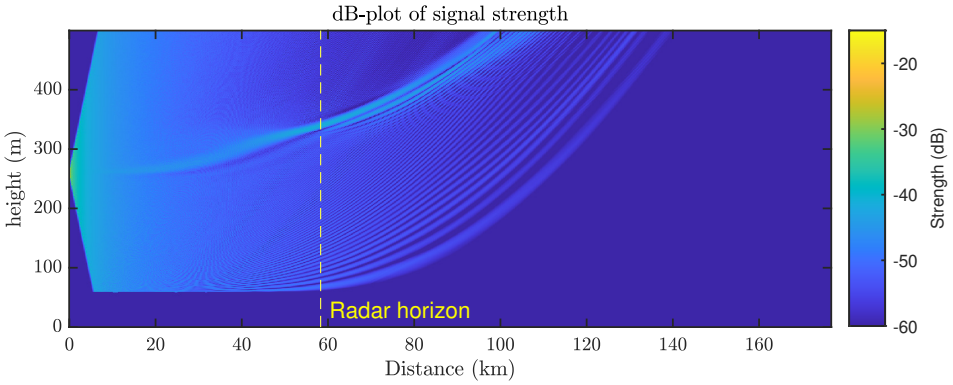

Figure 4.7: Plot of the wave propagation.

Chapter 5

Results, comparison and discussion

5.1 Results

This section presents plots of especially interesting areas, and how different radar parameters affect the propagation, with the assumption that the simulated propagation is correct. The data used for the simulations is the file

`CMEPSMLS_MBR000_202210180000+000H00M`, downloadable from SMHI's example data for MEPS [28]. A comparison is also made with the program PETOOL [24].

5.1.1 Comparing modified refractivity to refractivity

As mentioned in Section 2.3.3, the refractivity of the atmosphere is modified before simulation. This allows the approximation of a flat Earth surface, which keeps propagation in one direction, easing simulation. In order to visualize this, we choose a line west of Norway ($x_1 = 200,\ x_2 = 300,\ y_1 = 300,\ y_2 = 300$). As seen from Figure 5.1, this area closely follows the standard atmosphere. Attenuation is minimal with a propagation factor F of 0.9935.

Choosing a 0.5 GHz signal from an antenna 200 meters above the sea, with a beamwidth of 2 degress and no tilt, we simulate this both through modified refractive index (Figure 5.2) and regular refractive index (Figure 5.3). Comparing these two makes it clear that the modified refractivity bends the propagation away from the surface, in the same way that the surface would curve away from a propagating signal, if it would propagate over a spherical Earth.

5.1.2 Comparing propagation for different frequencies

Choosing the same area as in Section 4.4.2, we look at the propagation for different frequencies. Chosen frequencies are 3, 5, 8, 9, 13 and 15 GHz (as these occur in commercial sensor systems) as well as 22 GHz where we expect maximum attenuation. These simulations are presented in Figures 5.4-5.10. What can be seen from this is primarily how the interference pattern slims down for higher frequencies as well as how the range shorten, especially for 22 GHz. The shortened range of 22 GHz is from increased attenuation (the propagation factor for 22 GHz is 0.6846) while the pattern change is related to the shorter wavelength.

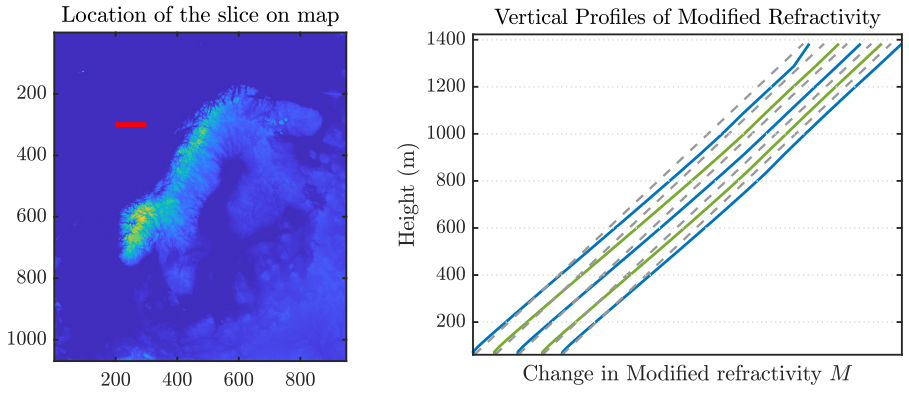

(a) Location of the slice on map **(b)** M-diagram along the slice. The dashed line represents a standard atmosphere

Figure 5.1: Location of the slice and M-diagram.

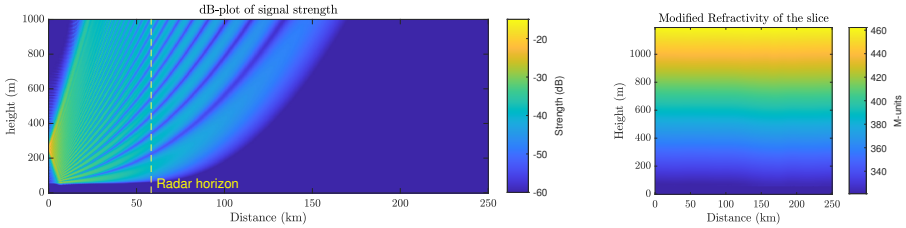

(a) Plot of the wave propagation **(b)** Modified Refractivity

Figure 5.2: The propagation and continuous refractivity profile.

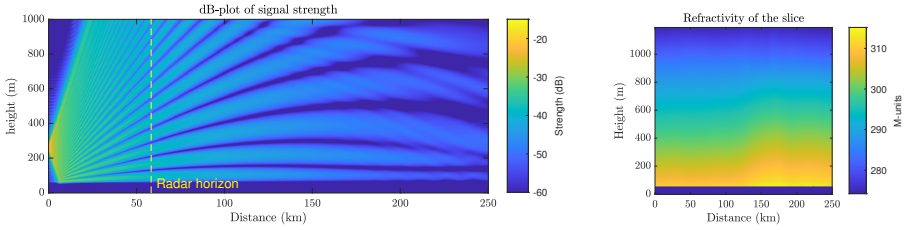

(a) Plot of the wave propagation **(b)** Refractivity

Figure 5.3: The propagation and continuous refractivity profile. Note that using this propagation would require a rounded Earth surface to be realistic.

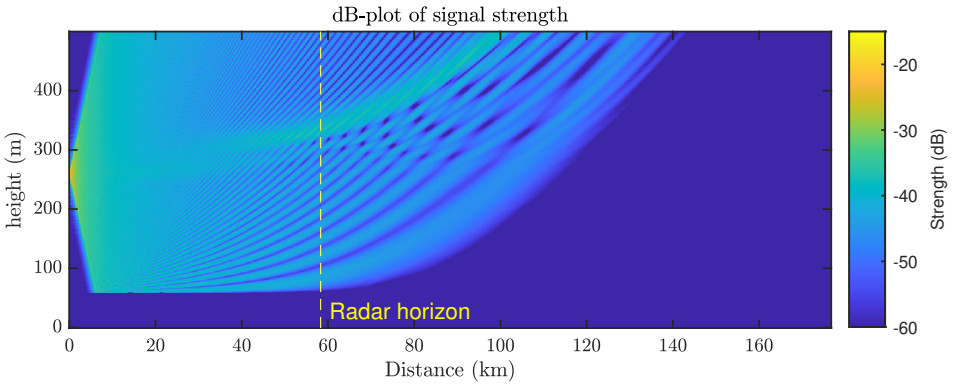

Figure 5.4: 3 GHz wave propagation.

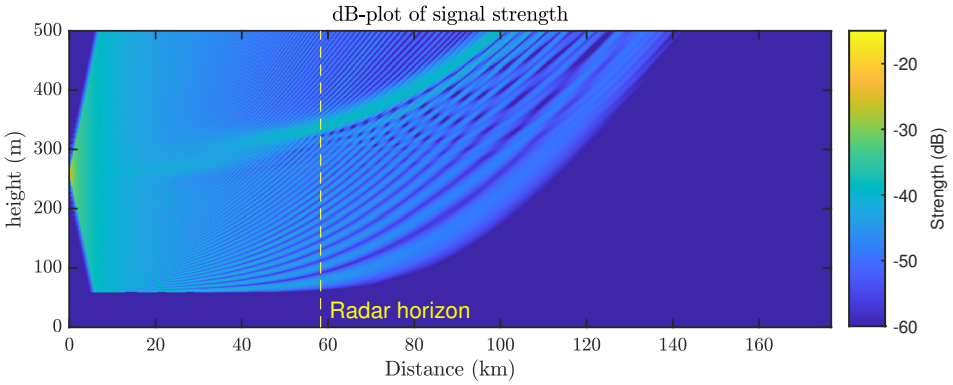

Figure 5.5: 5 GHz wave propagation.

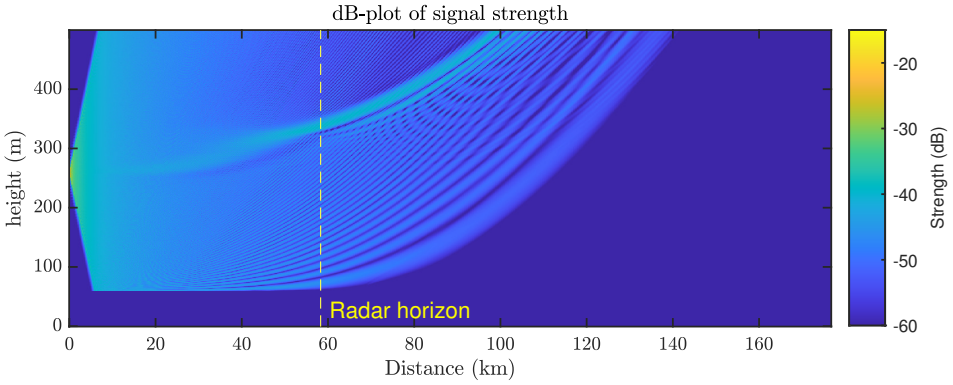

Figure 5.6: 8 GHz wave propagation.

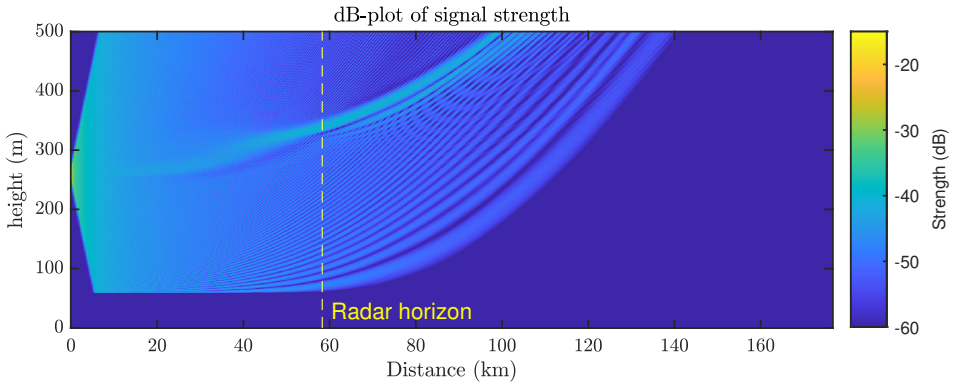

Figure 5.7: 9 GHz wave propagation.

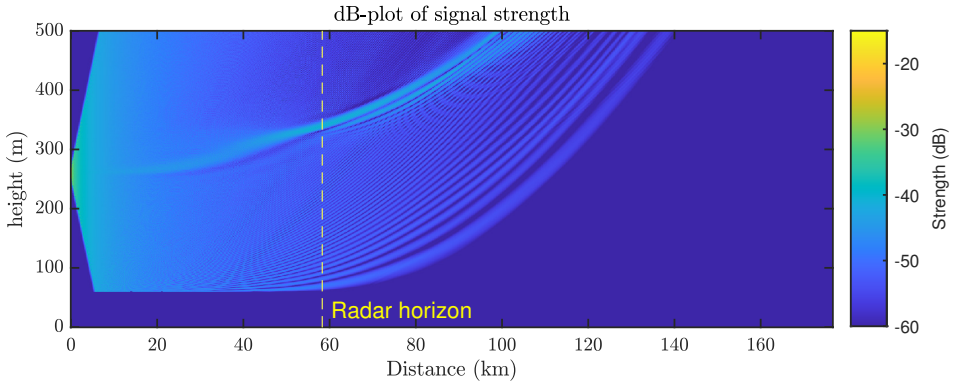

Figure 5.8: 13 GHz wave propagation.

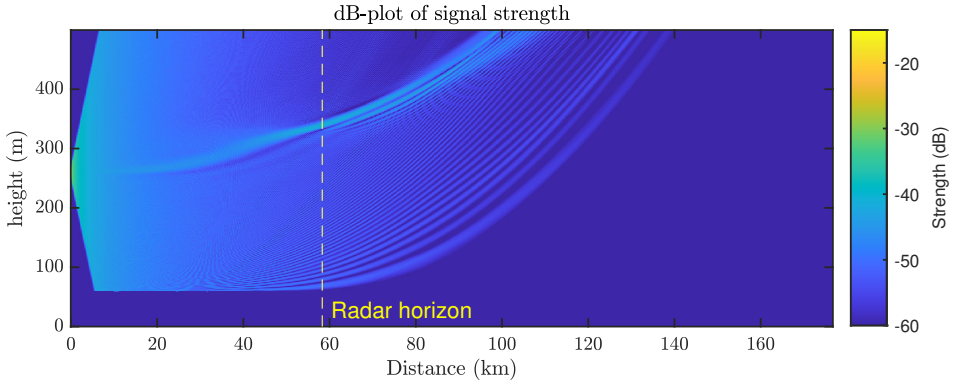

Figure 5.9: 15 GHz wave propagation.

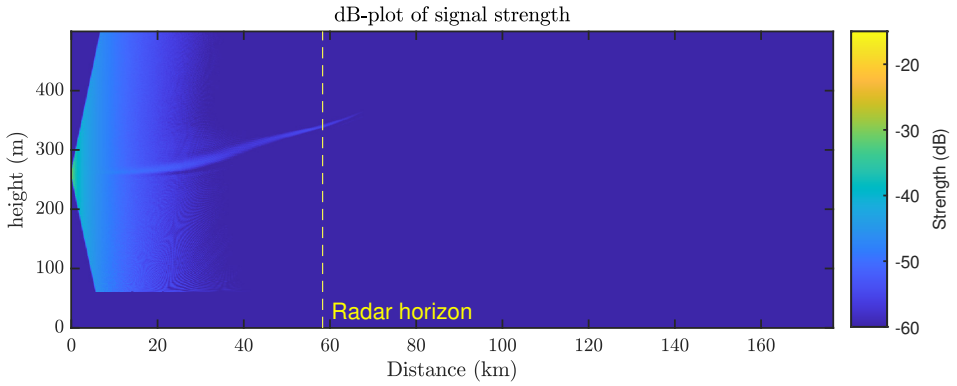

Figure 5.10: 22 GHz wave propagation.

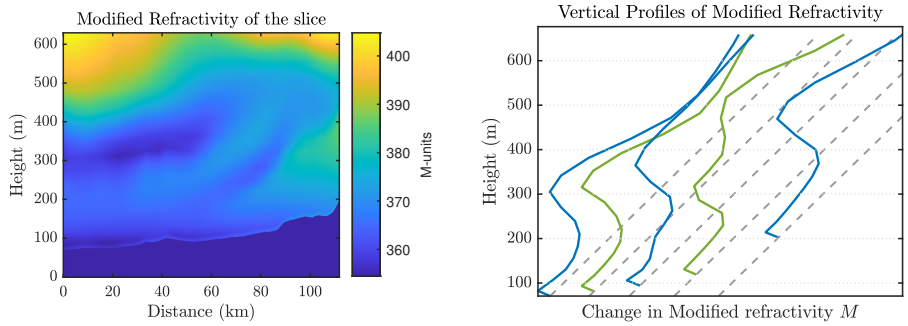

(a) Modified Refractivity **(b)** M-diagram

Figure 5.11: An interesting refractivity profile.

5.1.3 Comparing heights for an interesting area

Choosing an area further south, around the Netherlands ($x_1 = 200$, $x_2 = 240$, $y_1 = 1000$, $y_2 = 1020$), we find a more interesting refractivity profile, as seen in Figure 5.11 In the continuous profile a lot of small variations can be seen. Using the aide of the M-diagram an elevated duct can be found between 100 meters and 300 meters, continuing to around 50 km where it seems to split, with one part going further up and one part following the ground. Using this information we can begin by placing the source (15 GHz, beamwidth 2°, tilt 0°) inside the duct, at 170 meters. Here, in Figure 5.12, we can see the wave following the atmospheric ducts with the beginning of a split at 40 km.

Moving the source to 300 meters, we see effects of the top of the duct. Interestingly, Figure 5.13 indicates that positions along the ground that were in shadow before is now visible.

Finally, placing the source above the duct, at 400 meters, results in Figure 5.14 showing that signals can reach the ground even though there is a duct in the way.

Interested in more realistic scenarios, we position the source at 10 meters

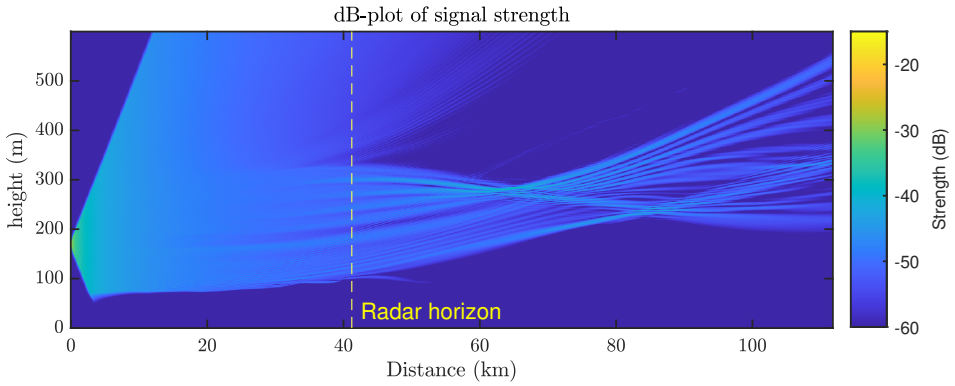

Figure 5.12: Antenna placed 100 meters above ground

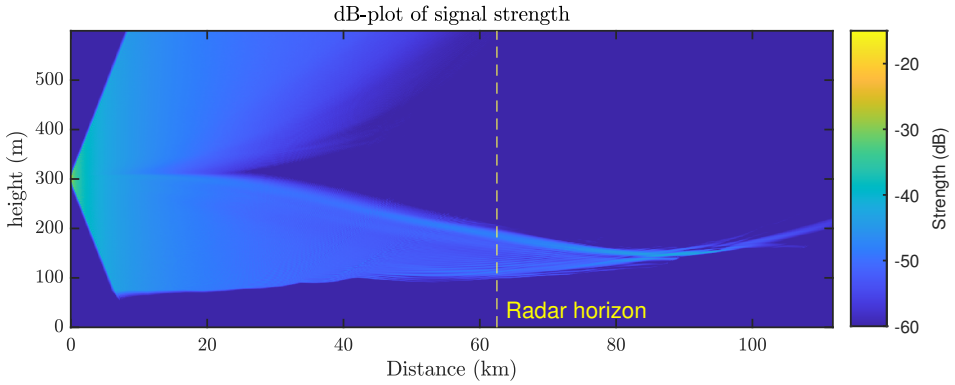

Figure 5.13: Antenna placed 230 meters above ground.

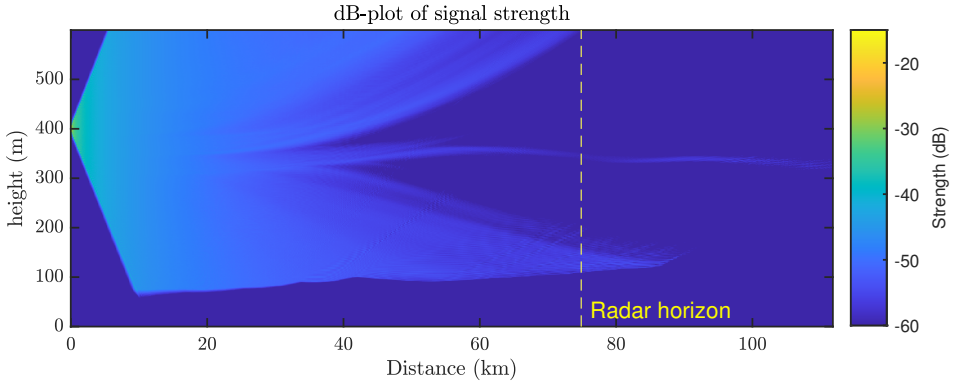

Figure 5.14: Antenna placed 330 meters above ground.

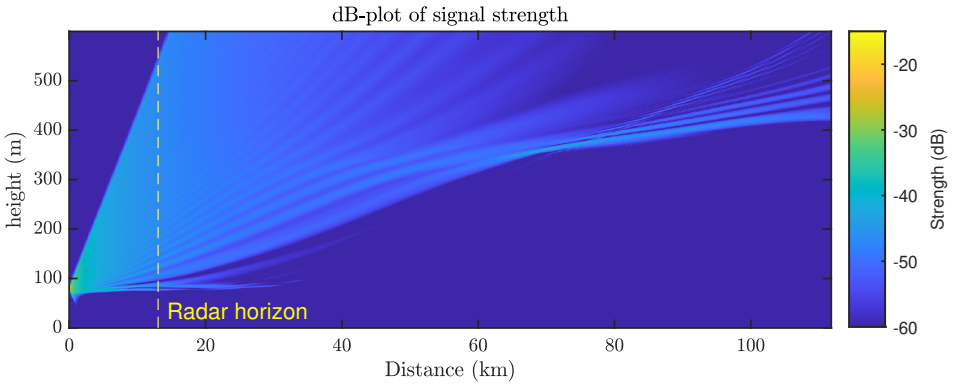

Figure 5.15: Antenna placed 10 meters above ground.

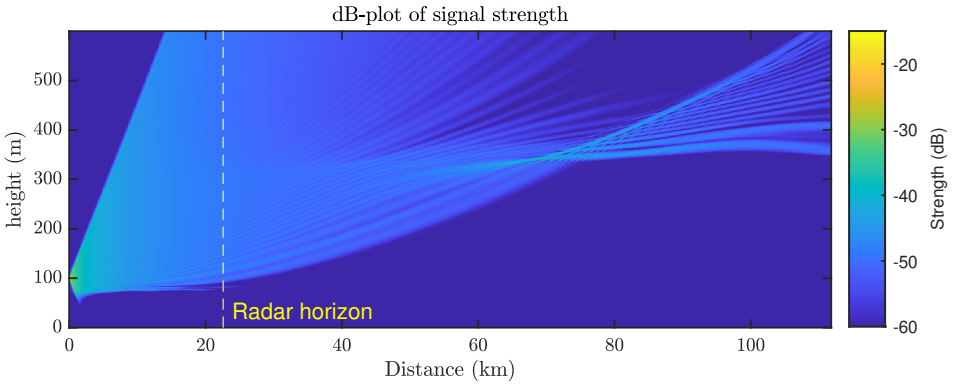

Figure 5.16: Antenna placed 30 meters above ground.

(Figure 5.15) and 30 meters (Figure 5.16) above the ground. Interesting for both of these is that while the radar horizon increases with antenna height, both show similar chances of observing flying objects at around 70 km away, or more than four times further than the horizon in the case for a 10 meter elevation.

5.1.4 Comparing the effects of attenuation

Choosing an area with a large cloud coverage according to Figure 4.4d and a frequency above 5 GHz, we can compare propagation with and without the propagation factor. A line is chosen close to Åbo in Finland ($x_1 = 613$, $x_2 = 550$, $y_1 = 600$, $y_2 = 600$) for which one gets the profiles in Figure 5.17. Simulating a 6 GHz source 10 meters above the ground with and without the propagation factor included in the SSPE returns Figure 5.18 and Figure 5.19. These figures show how the attenuation from clear air is manageable, but that the attenuation from clouds might weaken the signal too much for longer distances.

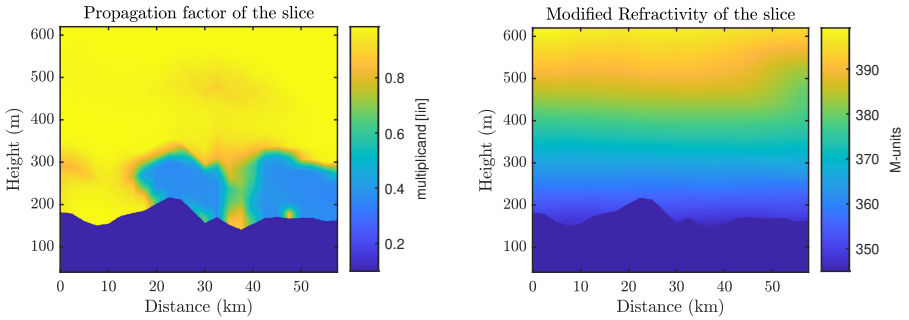

(a) Propagation factor F, $10^{-0.1\alpha \cdot dx}$ **(b)** Continuous Modified Refractivity

Figure 5.17: Propagation factor and refractivity for the chosen slice.

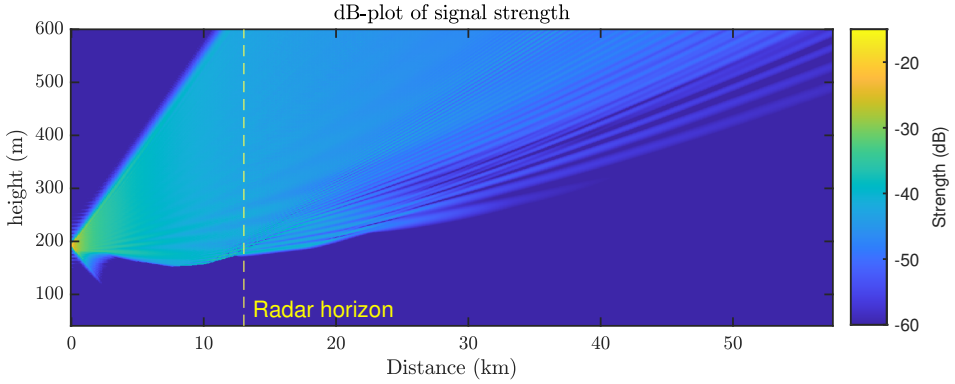

Figure 5.18: Antenna placed 10 meters above ground, attenuation included.

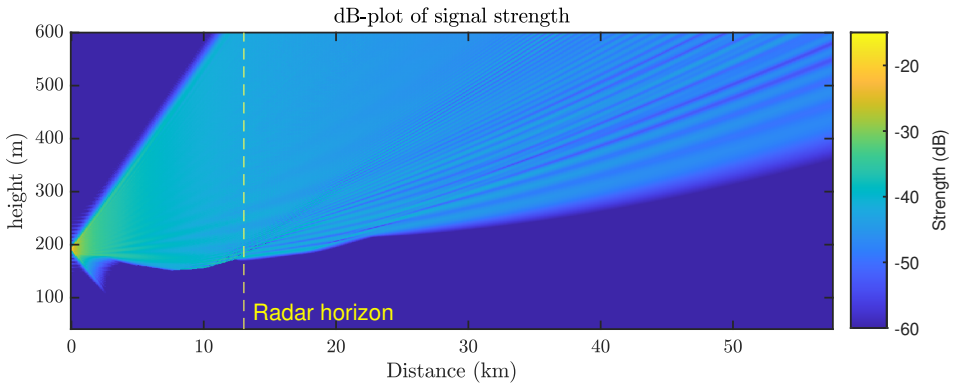

Figure 5.19: Antenna placed 10 meters above ground, attenuation excluded.

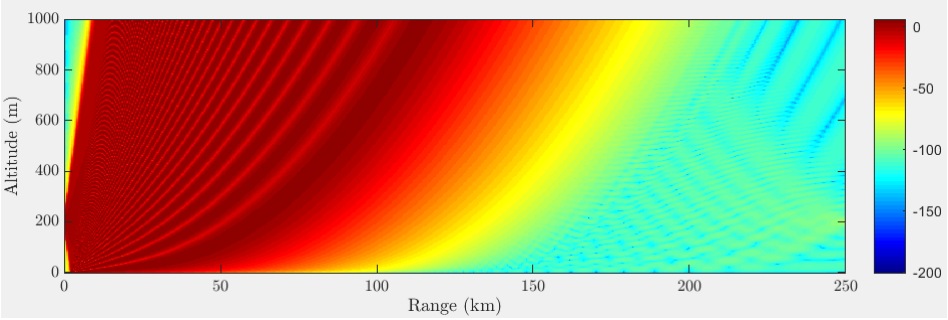

Figure 5.20: PETOOLs Propagation Factor for a standard atmosphere.

5.1.5 Comparison to other simulation software

While other available software do not readily allow for the input of weather data, the PETOOL developed by [24] allow the user to choose from different pre-defined atmospheric gradients, one of which is the standard atmosphere. Choosing the same source parameters, as well as the same refractivity, comparisons can be made to see how well the propagation predictor developed for this thesis corresponds to PETOOL.

Choosing the same area as in Section 5.1.1, we can remake the slice in PETOOL. Using the "standard atmosphere" starting at $M = 321$[-], setting the source to 0.5 GHz, with a beamwidth of 10°, tilt of 0°, an elevation of 200 m, $\Delta z = 1.9272$, $\Delta x = 100$ and the simulation area to 250[km] $\times$ 1000[m]. For boundaries the surface is set to the setting "sea". PETOOL returns the graph of Propagation Factor (PF) in Figure 5.20.

The values plotted can be exported from PETOOL and imported to the Propagation Predictor, allowing the plotting of both slices together, see the two upper plots Figure 5.21. According to [24], the PF is calculated as $\mathrm{PF} = 20\log(|u|) + 10\log(|x|) + 10\log(\lambda)$, with λ [m] being the wavelength and x [m] being the horizontal distance. What has so far been plotted by the Propagation Predictor is $20\log 10(|u|)$, so the PF from PETOOL is modified to match that. A new dynamic range (-20 to -250 dB) is also chosen for Figures 5.21 and 5.22 in order to accentuate small differences, such as the weak interference pattern to the right of the main one. The chosen dynamic range is inspired by Figure 5.20, though they differ slightly on account for Figure 5.20 showing $\mathrm{PF} = 20\log(|u|) + 10\log(|x|) + 10\log(\lambda)$ while Figure 5.21 and 5.22 show $20\log(|u|)$.

As seen from the top two slices in Figure 5.21, results do not match exactly. The large difference in values to the left of the main interference pattern is most likely because of differently modelled sources. Further right, the PETOOL graph appears to bend upward faster than the Propagation Predictor. This is mainly indicative of different values of (modified) refractive index, as that is the value controlling the deflection of the EM-wave.

Interested in why this difference occur, the SSPE equation is momentarily changed. Remembering the correct form, equation (3.14), the first part is changed

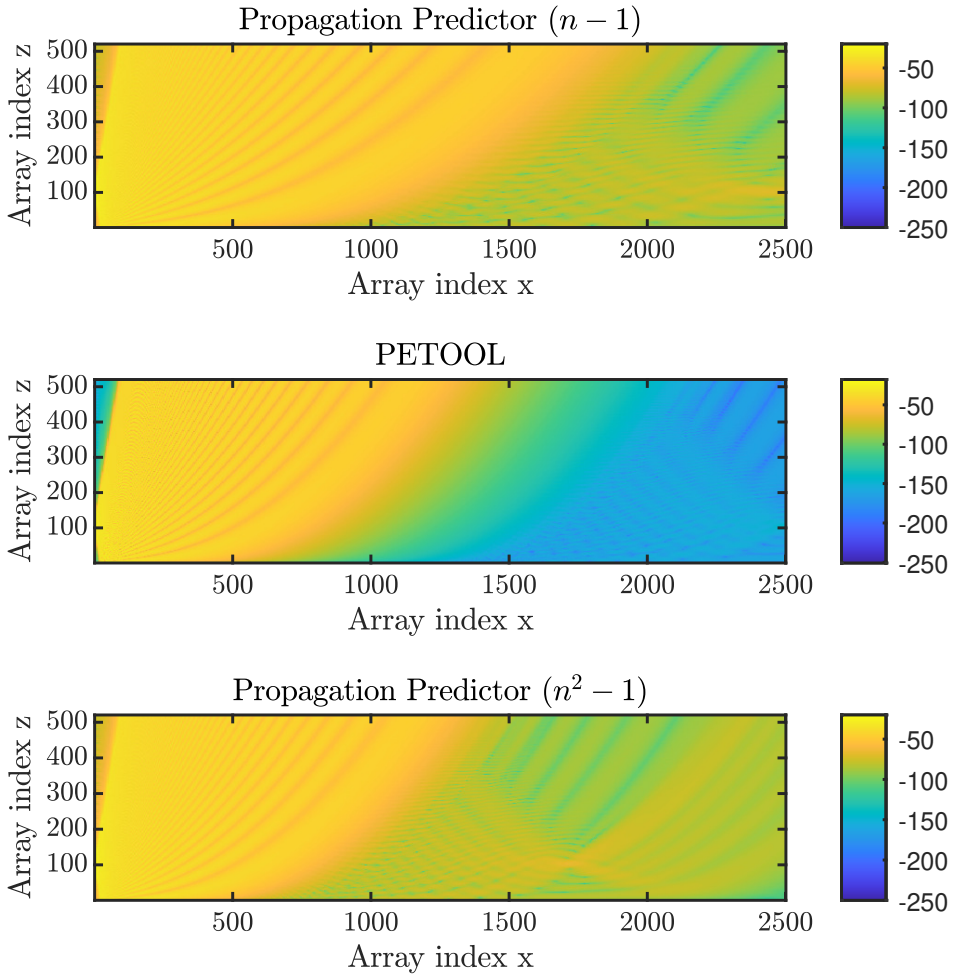

Figure 5.21: The three simulations plotted, all as $20\log(|u|)$. The Propagation Predictor $(n-1)$ corresponds to the correct WAPE implementation, with (n^2-1) corresponding the half of the correct NAPE implementation.

according to

$$e^{ik(n-1)\Delta x} \Rightarrow e^{ik(n^2-1)\Delta x} \tag{5.1}$$

which is half-way to the correct form of the NAPE, where this part instead is

$$e^{ik(n^2-1)\frac{\Delta x}{2}} \tag{5.2}$$

Doing the same simulation and comparison again, but now with the modification of (5.1), results in the lower plot in Figure 5.21. These results appear to correspond much better, at least for the main interference pattern.

The difference to the right of the main interference pattern probably comes from differently implemented boundaries, and in order to check this the simulation is run again with the $n^2 - 1$ modification, but with the window taper (the upper boundary) moved higher up. As seen in Figure 5.22, this moves the weaker pattern to the right as well as weakens it further, indicating that the pattern is from non-physical sky reflections. The lower plot in the same figure shows the effect of changed lower boundary.

While Figure 5.22 shows more similarities to PETOOL than previous figures, there is still a large difference in strength of the right-most area; approximately -170 dB for PETOOL and approximately -100 dB for the Propagation Predictor. By further decreasing reflections from the boundaries, this can be weakened and made to more closely resemble PETOOL, see Figure 5.23. Lowering the reflections from the lower boundary also weakens the main interference pattern.

By calculating the mean value of the graphs in Figure 5.21 for each range-step, a more qualitative comparison can be made. Plotting the difference between PETOOL and the propagation predictor (taking the mean of PETOOL value minus the mean value of the Propagation Predictor for each range step) results in Figure 5.24 and 5.25, where the latter shows the same data but more zoomed in.

5.2 Discussion

While the results look promising regarding the propagation through ducts and more complex refractivity profiles, the comparison with PETOOL suggests that some part of the simulation is off. While both simulations share inputs and simulation method (the wide angle SSPE), the interference pattern differ. It can be made to differ less by modifying the WAPE and the upper and lower boundary. While the lower boundary does not alter the overall shape of the main interference pattern, it does affect the strength and shape of the right-most area. Without having more access to the code for PETOOL it is difficult to ascertain exactly what causes these differences.

The waves in Figure 5.25 give an indication that the interference pattern does not match up exactly for neither (n^2-1) nor $(n-1)$. Zooming in to the graphs for Figure 5.22 show that the weaker values in the interference pattern reach the top of the graph roughly 15 index steps apart. This coincides well with the miniscule waves in Figure 5.25, which are also roughly 15 index steps from top to top. This is probably not because of simulation errors, but simply from mismatch when trying to align the results.

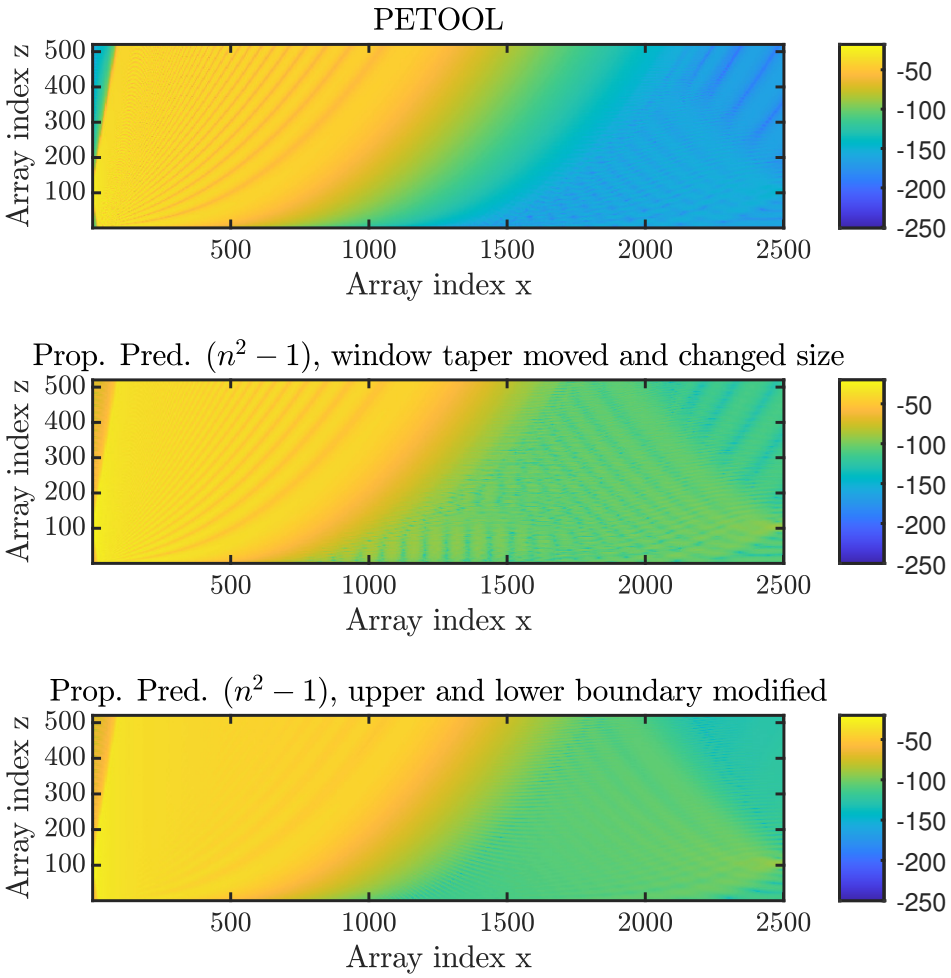

Figure 5.22: PETOOL compared to the modified propagation predictor. The window taper is moved further up than in previous simulations. The size is also smaller than usual, as a larger size fully removed the interference pattern to the right. In the lower plot the lower boundary is set to Land according to previous section.

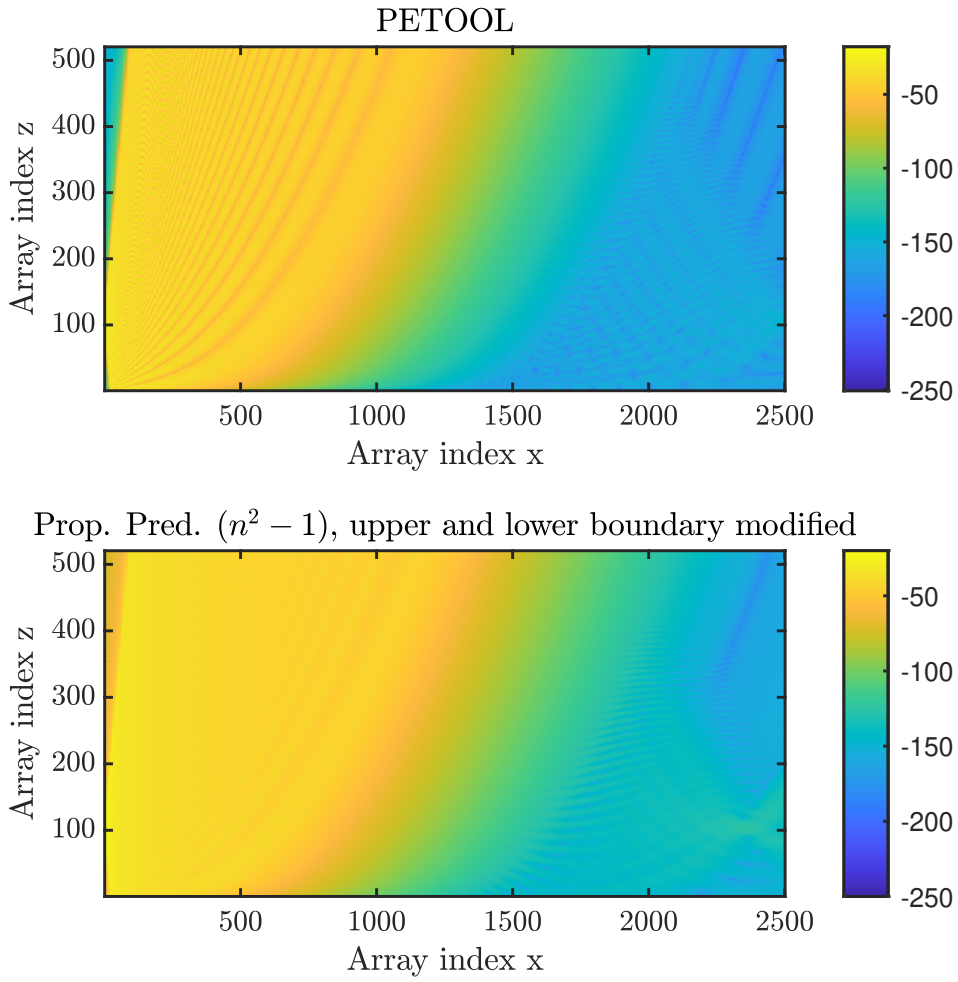

Figure 5.23: PETOOL compared to the modified propagation predictor. Boundaries are modified to minimize reflections.

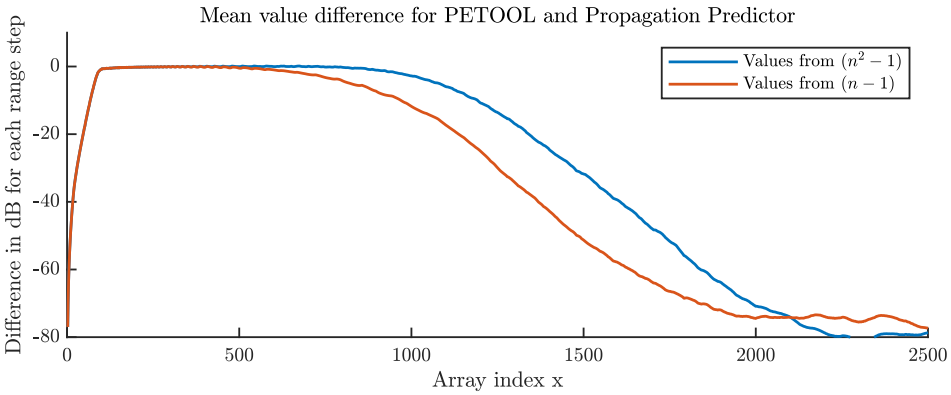

Figure 5.24: Differences in mean value between PETOOL and Propagation Predictor.

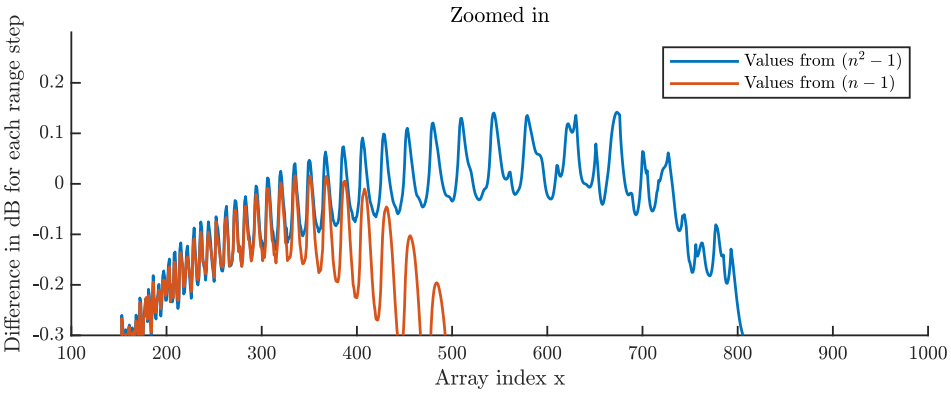

Figure 5.25: Differences in mean value between PETOOL and Propagation Predictor, zoomed in.

From Figures 5.12 to 5.14 it is interesting to see that while a duct can keep a signal along the ground (as in Figure 5.12), it will not necessarily block signals entirely in either direction. What might happen however is a shadow zone (here around 60km, 300m) which signals from multiple sources have difficulty reaching.

In addition to the attenuation already added, real-life propagation would include dispersion in the out-of-plane direction which is not included in the simulation. This means that the simulated wave retains more power than in a real world scenario, following $P \propto (2\pi \cdot \text{dist})^{-1}$ rather than $P \propto (4\pi \cdot \text{dist}^2)^{-1}$ in the regular one-way RRE.

5.3 Further research and improvements

In addition to double-checking the SSPE to find what differs from PETOOL, the following approaches could be worth taking in order to improve the propagation predictor.

5.3.1 Models for surface reflections

The boundary conditions for both ground and water are currently not modelled on actual physical behaviour. Having measurements and formulas for simulating this would improve accuracy. In addition to this, additional map data detailing what kind of ground (forest, marshes, field etc.) could also be beneficial.

5.3.2 Required thickness of layer

In [29] the author mentions that higher frequencies are more affected by the changing refractivity than lower frequencies. Likewise, course material made by the U.S. Naval Postgraduate school [30] claims that, in order for trapping to occur, the frequency of an incident EM-waves must be larger than a minimum frequency,

$$f_{\min} = \left(3.6 \cdot 10^5\right) d^{-3/2} \tag{5.3}$$

with thickness d in meter and frequency $f_{\min}$ in MHz. While not a citable source, this seems reasonable given the importance of electrical size, but proper measurements and verification would be necessary to say anything with certainty. In the context of the SSPE simulation this is irrelevant — the SSPE solves it anyway — but for a person reading M-diagrams it could be of help.

5.3.3 Including the ionosphere

While high up above the atmosphere and in general viable only for lower frequencies, flat enough grazing angle could allow higher frequencies to reflect down from the ionosphere. Currently, hybrid models of SSPE and RT are used to simulate propagation all the way to the ionosphere, though the Swedish Defence Research Agency (FOI) have published an article regarding use of only SSPE for the entire height [31], showing promising results. Theoretically it should not be too difficult to implement here either; continue the refractivity slice for as long as data allow,

then decrease further with height until the ionosphere starts, and there use the formulas for ionospheric refractivity. It will however require large internal memory and large calculations, unless some clever work-around can be made.

5.3.4 Other meteorological sources

As seen in Table 2.3, MEPS is one of many meteorological data sources. Incorporating other sources could both increase viable regions for simulation, as well as offer a "second opinion" on already available areas. This will however require extra work, as all models work a little differently. Also incorporating API support for downloads would increase user experience.

5.3.5 Proper coordinate input

In order to incorperate map data or to communicate locations properly, use of latitude och longitude would be beneficial. Regarding MEPS there is Python-code available for converting the Lambert projection used, so a MATLAB implementation should be fairly straight forward.

Chapter 6
Conclusions

This thesis shows that it is possible to use meteorological data as a basis for propagation of EM-waves using the SSPE. The SSPE is well used in similar projects as it offers accurate results while being fairly non-demanding of hardware. While comparisons indicate that results in this thesis do not match already published implementations, these differences appear to be quick and easy to fix.

Being able to use the same meteorological data for refractive index, attenuation, elevation and ground type is a major benefit when it comes to usability, as this eliminates compatibility issues that could arise when dealing with different data sources. Variations in refractive index can occur both vertically and horizontally without breaking the simulation, though large horizontal gradients will demand shorter range steps. The modelling of surfaces are currently lacking a physical basis, though they are probably good enough.

In summary, using meteorological data and simulating wave propagation with the SSPE should not be taken for absolute truth, but is likely in the ball park of what is correct. Given its ease of use and quick simulation time, it fills its role well as real-time sanity check.

References

[1] J. Lilensten and J. Bornarel, *Space Weather, Environment and Societies*. Springer Dordrecht, 2006.

[2] B. R. Bean, U. S. N. B. of Standards., and E. J. Dutton, *Radio meteorology*. Gaithersburg, MD: U.S. Dept. of Commerce, National Institute of Standards and Technology;, 1966.

[3] M. A. Richards, J. A. Scheer, and W. A. Holm, *Principles of Modern Radar : Basic Principles*. Institution of Engineering Technology, ProQuest Ebook Central, 2010, vol. 1. [Online]. Available: https://ebookcentral.proquest.com/lib/lund/detail.action?docID=3012285

[4] A. Öbrink. Försvarets nya radar ska ge tidig varning om hot. Retrieved 2026-02-07. [Online]. Available: https://www.svt.se/nyheter/inrikes/forsvarets-nya-radar-ska-ge-tidig-varning-om-hot

[5] L. Norin, N. Wellander, and A. Devasthale, "Anomalous propagation and the sinking of the Russian warship Moskva," *Bulletin of the American Meteorological Society*, vol. 104, no. 12, pp. E2286 – E2304, 2023. [Online]. Available: https://journals.ametsoc.org/view/journals/bams/104/12/BAMS-D-23-0113.1.xml

[6] G. Jönsson, *Våglära och optik*, 7th ed. Teach Support, 2018.

[7] D. J. Griffiths, *Introduction to Electrodynamics*, 4th ed. Cambridge University Press, 2017.

[8] L. Norin, "Observations of anomalous propagation over waters near Sweden," *Atmospheric Measurement Techniques*, vol. 16, no. 7, pp. 1789–1801, 2023. [Online]. Available: https://amt.copernicus.org/articles/16/1789/2023/

[9] P. Davis, G. Parbrook, and G. Kenny, "Chapter 12 - humidification," in *Basic Physics and Measurement in Anaesthesia (Fourth Edition)*, fourth edition ed., P. Davis, G. Parbrook, and G. Kenny, Eds. Butterworth-Heinemann, 1995, pp. 146–157. [Online]. Available: https://www.sciencedirect.com/science/article/pii/B9780750617130500172

[10] SMHI. Atmosfärens olika lager. Retrieved 2025-10-02. [Online]. Available: https://www.smhi.se/kunskapsbanken/meteorologi/atmosfarens-cirkulation/atmosfarens-olika-lager

[11] ——. Inversion. Retrieved 2025-10-27. [Online]. Available: https://www.smhi.se/kunskapsbanken/meteorologi/atmosfarens-cirkulation/inversion

[12] E. Karlsson, B. Asp, G. Eriksson, and M. Rundgren, "Vågutbredningsanalys för radio och radar. Förstudie." Totalförsvarets forskningsinstitut FOI, Tech. Rep., 2001.

[13] L. Ladell, "Strålbaneberäkning och radarräckvidd," Försvarets forskningsanstalt FOA, Tech. Rep., 1989.

[14] S. Wickerts, "Multipath propagation at 11, 18 and 36 GHz due to ducting," Försvarets Forskningsanstalt FOA, Tech. Rep., 1983.

[15] A. Komjathy, "Ionospheric effects on the propagation of electromagnetic waves," in *Encyclopedia of remote sensing*, E. G. Njoku, Ed. Springer, 2014.

[16] S. J. Orfanidis, *Electromagnetic waves and antennas.* Rutgers University, 2016.

[17] O. Gustafsson, G. Eriksson, P. Holm, A. Hågård, E. Karlsson, M. Nordstrand, R. Persson, P. von Schoenberg, and Åsa Waern, "Slutrapport för projektet vågutbredningsanalys för radio, radar och elektrooptiska system," FOI, Tech. Rep., 2003.

[18] O. Gustafsson, G. Eriksson, P. Holm, R. Persson, L. Thaning, P. von Schoenberg, and Åsa Waern, "Slutrapport för projektet verifiering av vågutbredningsmodeller," FOI, Tech. Rep., 2006.

[19] S. Wickerts, "Metodik att ur meteorologiska data bestämma förekomst av ledskikt," Försvarets Forskningsanstalt FOA, Tech. Rep., 1966.

[20] E. Olsson, Oct 2025, private communication.

[21] G. Dockery, "Modeling electromagnetic wave propagation in the troposphere using the parabolic equation," *IEEE Transactions on Antennas and Propagation*, vol. 36, no. 10, pp. 1464–1470, 1988.

[22] F. D. Tappert, *The parabolic approximation method.* Berlin, Heidelberg: Springer Berlin Heidelberg, 1977, pp. 224–287. [Online]. Available: https://doi.org/10.1007/3-540-08527-0_5

[23] D. Dockery and J. Kuttler, "An improved impedance-boundary algorithm for Fourier split-step solutions of the parabolic wave equation," *IEEE Transactions on Antennas and Propagation*, vol. 44, no. 12, pp. 1592–1599, 1996.

[24] O. Ozgun, G. Apaydin, M. Kuzuoglu, and L. Sevgi, "Petool: Matlab-based one-way and two-way split-step parabolic equation tool for radiowave propagation over variable terrain," *Computer Physics Communications*, vol. 182, no. 12, pp. 2638–2654, 2011. [Online]. Available: https://www.sciencedirect.com/science/article/pii/S0010465511002669

[25] L. Hörmander, *The Analysis of Linear Partial Differential Operators III Pseudo-Differential Operators.* Springer, 2007.

[26] D. J. Thomson and N. R. Chapman, "A wide-angle split-step algorithm for the parabolic equation," *The Journal of the Acoustical Society of America*, vol. 74, no. 6, pp. 1848–1854, 12 1983. [Online]. Available: https://doi.org/10.1121/1.390272

[27] SMHI. Meteorologisk modell (meps) - prognosdata realtid. Retrieved 2025-10-14. [Online]. Available: https://www.smhi.se/data/sok-oppna-data-i-utforskaren/meteorologisk-modell-meps-prognosdata-realtid

[28] ——. Index of /data/example_files/meteorology/cmeps. Retrieved 2026-02-06. [Online]. Available: https://data-download.smhi.se/data/example_files/meteorology/cmeps/

[29] H. V. Hitney, J. H. Richter, R. A. Pappert, K. D. Andersson, and G. B. BaumgartnerJr, "Tropospheric radio propagation assessment," in *Proceedings of the IEEE, Vol. 83, No. 2*, February 1985.

[30] Types of ducts. Retrieved 2026-02-07. [Online]. Available: https://www.oc.nps.edu/NWDC_EM_Course/course_materials/module3_2.html

[31] M. Elenius, E. Corrigan, and G. Eriksson, "HF propagation modelling with parabolic equation techniques," in *Nordic shortwave conference*, R. Berg, Ed. NRS, August 2025. [Online]. Available: nordichf.org

Appendix A

Sammanfattning

Atmosfärens brytningsindex beror på dess tryck, luftfuktighet och temperatur. När dessa ändras i höjdled leder detta till en brytningsindexsgradient som kan böja elektromagnetisk strålning i radiospektrat. Vid så kallad standardatmosfär böjs strålningen lite nedåt marken; det är detta som ligger till grund för att använda 4/3 jordradie vid beräkning av radarräckvidd. Atmosfären skiljer sig dock ganska ofta från standard vilket kan leda till undernormal och övernormal brytning, samt ledskikt.

A.1 Att tolka M-diagram

M-diagram visar hur brytningsindexet i atmosfären varierar med höjden. Att läsa av det för hand kan ge en fingervisning av hur vågorna kommer utbreda sig men missar samtidigt en hel del viktiga delar, exempelvis interferensmönstret som bildas av reflektioner i marken.

Om M är konstant med höjden, det vill säga att grafen går rakt uppåt, så föreligger chans för ledskikt. Oftast krävs det dock ganska kraftig lutning åt vänster, alltså att M minskar kraftigt med höjden. En lutning åt höger på 118 M per meter motsvarar en standardatmosfär. I sådana fall gäller approximationen om 4/3-jordradie. I figur 2.8 visas olika typexempel av M-diagram, och i figur 5.11 finns ett exempel från inläst väderdata.

A.2 Tecken på ledskikt i verkligheten

Ledskikt kan som tidigare nämnts uppstå av ett med höjden kraftigt avtagande brytningsindex. Brytningsindex påverkas starkast av luftfuktigheten vilket innebär att ledskikt ofta uppstår då luftfuktighet avtar kraftigt med höjden. I vissa fall kan detta ses med blotta ögat, exempelvis som den övre gränsen av ett moln eller av lågt svävande dimma. Problemet med dessa fenomen är att vattenångan samtidigt riskerar att dämpa strålningen kraftigt, beroende på strålningens frekvens.

A.3 Ledskikt som energifälla

Att en våg utbreder sig längre i ledskikt beror inte enbart av att den kröks längst med jordytan och därav får en mer avlägsen horisont. Ledskiktet hindrar även spridning i vertikal led vilket innebär att den typiska spridningen $1/R^2$ istället blir $1/R$. Detta kan jämföras med en en-dimensionell vågledare.

A.4 Antennjusteringar

Att justera elevationsvinkel eller strålbredd har i regel inte särskilt stor påverkan på vågubredningen; på tillräckligt långa distanser täcks flera hundra höjdmeter oavsett om strålbredden är 0.1 eller 1 grad. Det som istället kan ha stor påverkan är höjden på sensorn. Att placera sensorn mitt i gränsen för ett ledskikt döljer ofta föremål på nära håll och på samma höjd men kan istället tillåta god sikt nära markytan långt bortom radarhorisonten. Det är alltid värt att simulera vågutbredningen för flera höjder.

Appendix B

Svensk-engelsk ordbok

Ducting Ledskikt

Elevated duct Höjdledskikt

Fading Fädning

Ground-based ducting Markbaserade ledskikt

High-pressure areas Högtrycksområden

Modified refractivity Modifierad brytningsmodul

Optical path Strålgång

Partial pressure of water vapour Vattenångans tryck

Propagation Utbredning

Ray optics Stråloptik

Refractive index Brytningsindex

Refractivity Brytningsmodul

Standard deflection Normal brytning

Sub-deflection Undernormal brytning

Super-deflection Övernormal brytning

Surface-based duct Markbaserat ledskikt

Surface duct Markledskikt

Trapping Fångning

Trapping layer Spärrskikt

Appendix C

SSPE code

The MATLAB code used for simulating the propagation. Note that `lambda`, `n`, `atten`, `ground`, `heightRange`, `vertRange`, `elevationAboveGround`, `tilt` and `beamWidth` are inputs from previous parts of the program.

```
disp('running SSPE')
% Constants
k0 = 2*pi/lambda;     % Free space wavenumber

%Simulation space
dz=heightRange(2)-heightRange(1);
Nz=length(heightRange);
zvec = heightRange-min(heightRange);

dx=vertRange(2)-vertRange(1);
Nx=length(vertRange);

%Is different for even or odd Nz,
%but Nyquist is more consistent when even
%and makeSlice only gives even
p = 2*pi * [0:(Nz/2-1), (-Nz/2):-1] / (Nz * dz);

%total elevation above ground
totHeight = elevationAboveGround+find(isnan(n(1,:)),1,'last')*dz;
if isempty(totHeight) %if antenna is on lowest part of slice
    totHeight=elevationAboveGround;
else
end

%initial field
antPos = zvec-totHeight;

alpha=0.1102*(60-21); %60db according to Thomson83
beta = sqrt(1-((antPos)./(max(zvec)-totHeight)).^2);

u0=sqrt(lambda)./(pi*(antPos)).*sin(2*pi./lambda.*antPos.* ...
```

```
    tand(beamwidth)).*besseli(0,alpha.*beta)./besseli(0,alpha);

u0=u0.*exp(-1i*k0*sind(tilt).*zvec); %modify for tilt

u = zeros(Nx, Nz); %pre-allocate for efficiency
u(1,:) = u0; %initial value

%window function
window=ones(1,Nz);
holder = hann(399);
%creates a x long Hann-window from 1 to 0. used for the extra 100dz
skyfade = holder(200:end);
window(end-199:end) = skyfade;

tic
for j=1:(Nx-1)
    if(ground(j))==1 %land
        n(j,isnan(n(j,:)))=n(j,sum(isnan(n(j,:)))+1)+1i*1e-5;
    else %water
        n(j,isnan(n(j,:)))=n(j,sum(isnan(n(j,:)))+1)+1i*1e-3;
    end

    u(j+1,:) = exp(1i*k0*(n(j,:) - 1)*dx).* ...
        ifft(exp(-1i*p.^2*dx./(sqrt(k0^2 - p.^2) + k0)).* ...
        fft(u(j,:).*window.*10.^(0.1.*-atten(j,:).*dx)));

end
toc

u=u./sqrt(sum(abs(u0).^2)); %normalize so that initial total energy is 1

end
```

Printed by Tryckeriet i E-huset, Lund 2026

LUND
UNIVERSITY

Series of Master's theses
Department of Electrical and Information Technology
LU/LTH-EIT 2026-1119
http://www.eit.lth.se